Planetary and Space Science 188 (2020) 104936

Contents lists available at ScienceDirect

Planetary and Space Science

journal homepage: www.elsevier.com/locate/pss

A comparative study of radar and optical observations of meteor showers using SAAMER-OS and CAMS

Juan Sebastián Bruzzone [a,b,*], Diego Janches [b], Peter Jenniskens [c,d], Robert Weryk [e], Jose Luis Hormaechea [f,g]

[a] Department of Physics, Catholic University of America, 620 Michigan Ave., N.E. Washington, DC, 20064, USA
[b] ITM Physics Laboratory, NASA Goddard Space Flight Center, Code 675, 8800 Greenbelt Rd, Greenbelt, MD, 20771, USA
[c] SETI Institute, 189 Bernardo Ave, Mountain View, CA, 94043, USA
[d] NASA Ames Research Center, Mail Stop 244-11, Moffett Field, CA, 94035, USA
[e] Institute for Astronomy, University of Hawaii, 2680 Woodlawn Drive, Honolulu, HI, 96822, USA
[f] Facultad de Ciencias Astronomicas y Geofisicas, Universidad Nacional de, La Plata, Argentina
[g] Estacion Astronomica Rio Grande, Rio Grande, Tierra del Fuego, Argentina

ARTICLEINFO

Keywords:
Meteoroids
Meteors
Radar
Video

ABSTRACT

We present a comparison of radar and optical meteor shower radiant distributions with the Southern Argentina Agile Meteor Radar-Orbital System (SAAMER-OS) and the Cameras for Allsky Meteor Surveillance (CAMS). This study comprise seven years of meteor radar surveillance with SAAMER-OS and over eight years of the CAMS video meteor data. In total, over five million meteor radar and close to 500,000 video meteor orbits are analyzed thus providing a robust statistical dataset. With a five-fold increase in SAAMER-OS orbits, we revisit the initial SAAMER-OS shower survey and compare a selection of 20 established meteor showers against those reported by CAMS.

1. Introduction

The dust content in the inner solar system can be probed by radar and video observations of meteors in the atmosphere and provide a reliable way to examine the dissemination of material populating the Zodiacal Dust Cloud (ZDC). Radar and video observations sample two size regimes of the debris population. Through the cumulative record of observed meteoroid orbits, a clearer picture of the true distribution of the interplanetary debris is presented, shedding light into the origin of the parent bodies of the meteoroid population, namely asteroids and comets (Jenniskens, 2006).

Meteoroids and dust ejected from comets approaching the inner solar system is the main source of particles in meteoroid streams, many of which result in the meteor showers seen at Earth (Jenniskens, 2008; Nesvorny et al., 2010). The fresh materials ejected retain the history of their parent body due to their relative low ejection speed making the observation of meteor showers an excellent tool to constrain dynamical models of cometary evolution. Also important is the influx of evolved sporadic meteoroids which over time have lost their history and thus cannot be associated to a parent object. Over the years, radar and video observations have gathered large number of meteoroid orbits enabling the identification of the main sources of meteoroid material arriving at Earth for both meteoroid streams and sporadic sources (e.g. Hawkins, 1963; Jenniskens, 1994; Galligan and Baggaley, 2002; Brown et al., 2008, 2010; Jenniskens et al., 2011, 2012; Janches et al., 2014; Pokorný et al., 2017).

As every measuring technique, radar and video observations are subject to biases and measurement error (Jenniskens et al., 2011; Janches et al., 2014). Radar surveys are usually sensitive to fainter meteoroids arising from meteoroids in the sub-mm size regime. Different radars have large difference in sensitivities and thus the type of echo they can detect (i.e. head vs trail) and the size range depends strongly on transmitted power and system aperture (Janches et al., 2014, 2015). The number of meteoroids over a single radar site well surpasses that of the less-frequently-occurring larger cm-sized meteoroids detected by video, often resulting in larger data sets. Also, radar surveys have the capacity of uninterrupted daily operations which enables observing meteors from the helion source. In spite of the frequently bigger observation sample, our study suggest that radiant measurement errors could be a factor of 2 larger on average. On the contrary, video observations offer higher

* Corresponding author. Department of Physics, Catholic University of America, 620 Michigan Ave., N.E. Washington, DC, 20064, USA.
E-mail address: juan.s.bruzzone@nasa.gov (J.S. Bruzzone).

https://doi.org/10.1016/j.pss.2020.104936
Received 15 November 2019; Received in revised form 13 February 2020; Accepted 10 April 2020
Available online 12 May 2020
0032-0633/

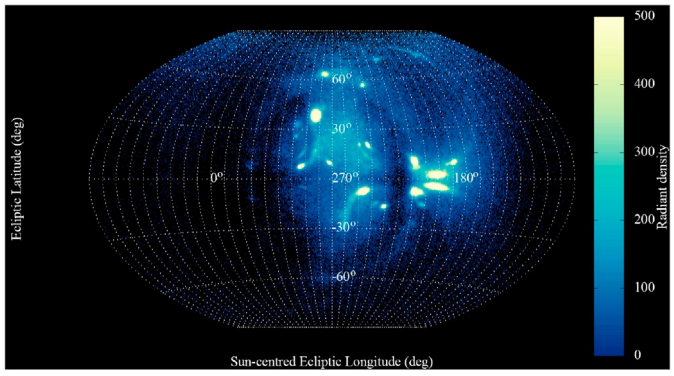

Fig. 1. Meteor radiant density plot in sun-centered ecliptic coordinates of eight years of video meteor surveillance with CAMS. Radiant density is estimated as number of meteors within 1.0°

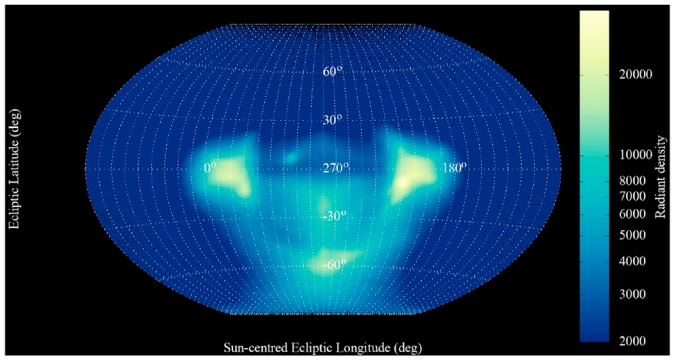

Fig. 2. Meteor radiant density plot including seven years of the SAAMER-OS meteoroid orbit survey in sun-centered ecliptic coordinates. Radiant density is computed as the number of meteors within 2.8°.

angular and velocity resolution resulting in individual meteoroid orbits being better defined. Also, mm-sized meteor showers are more prominent relative to the weaker sporadic background. However, optical surveys naturally suffer from the diurnal cycle and local weather conditions often limiting the sky coverage to regions roughly 20° away from the Sun. This together with the fact that mostly detect meteors produced by larger meteoroids than the radars result in significantly smaller data sets.

Because of the different detection rates, the data analysis of radar and optical observations is often approached in different ways. Here, we aim to present a consistent approach to study the detection of meteor showers and to better compare results from two different observing techniques that are usually sensitive to different aspects of meteoroid streams. To this end, this paper focus on employing a wavelet transform-based methodology to isolate and compute the mean orbital elements of meteoroid streams and to compare results from two surveys, the radar-based SAAMER-OS and optical CAMS meteor orbit surveys. Our methodology offers an unified procedure to compare and characterize meteor showers as seen by radar and optical techniques.

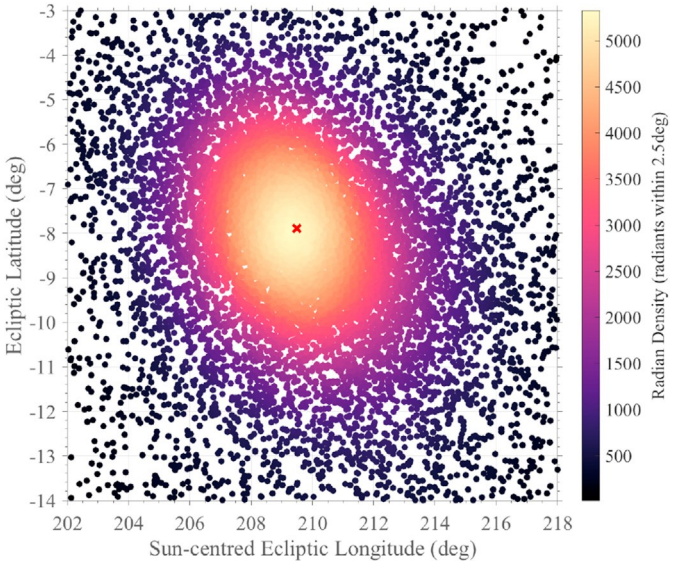

Fig. 4. Radiant plot of SDA meteors observed with SAAMER-OS. Radiants are color-coded by radiant density. Radiants were extracted at $\lambda_\odot$ 125°. (For interpretation of the references to color in this figure legend, the reader is referred to the Web version of this article.)

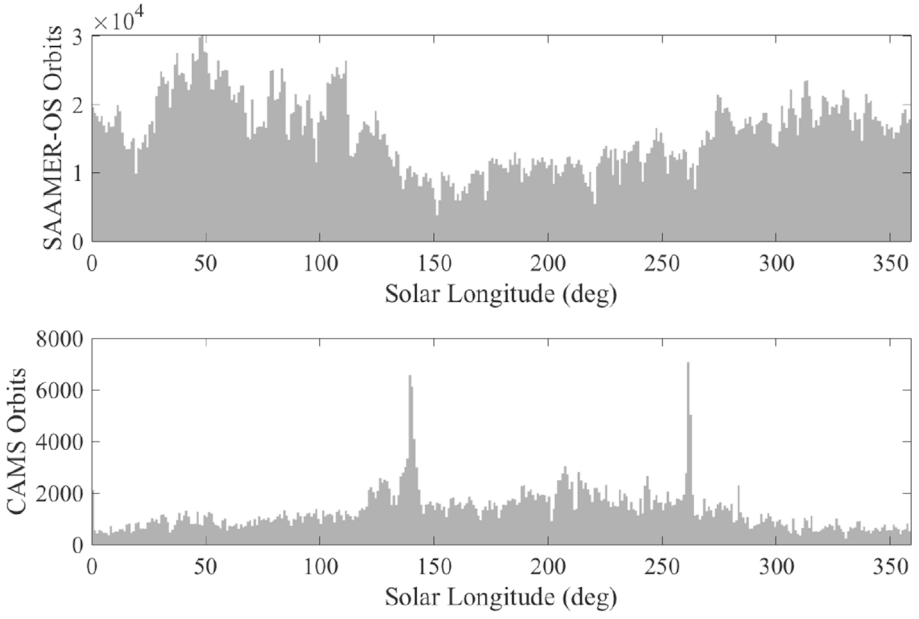

Fig. 3. Number of orbits per degree of solar longitude for seven years of the SAAMER-OS meteoroid orbit survey and eight years of CAMS video meteor surveilance.

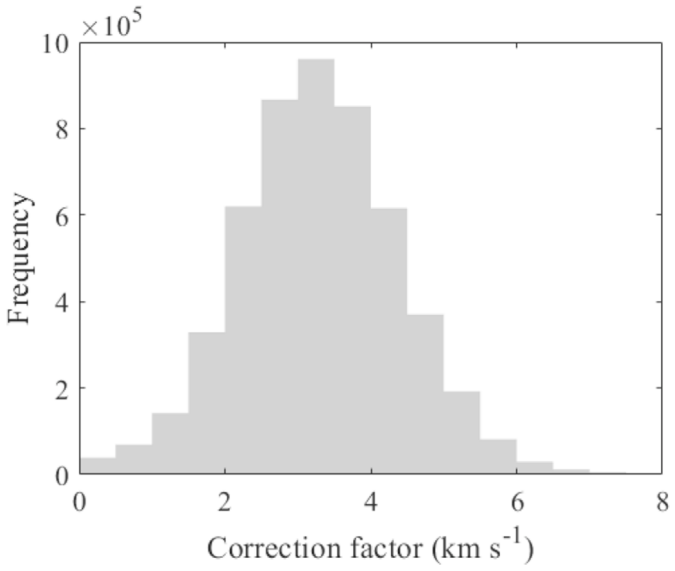

Fig. 5. Distribution of correction factors resulting from Equation (2) for SAAMER-OS meteors.

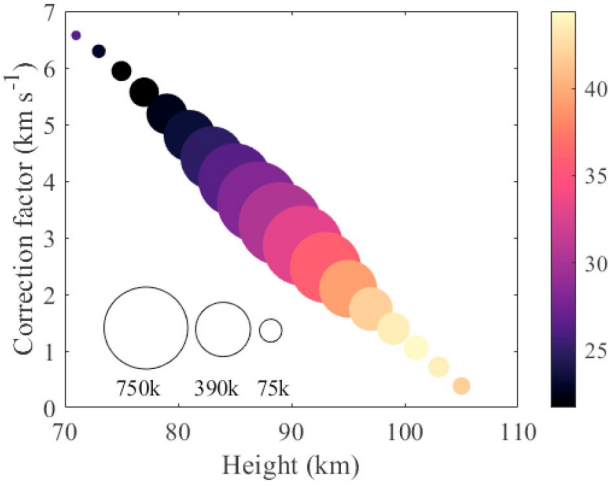

Fig. 6. Correction factors resulting from Equation (2) as a function of meteor height for SAAMER-OS. Median correction factors and median speeds are estimated at 2 km-wide height bins. Datapoints are color coded by median meteor speed in km s^{-1} and datapoint sizes represent number of meteors within each height bin. (For interpretation of the references to color in this figure legend, the reader is referred to the Web version of this article.)

A description of the survey instruments used in this study is presented in Section 2. Section 3 presents the treatment of the deceleration correction for radar observations, an introduction to the wavelet-based methodology and results for the identified meteor showers. Section 4 pertains to the discussion while conclusions are presented in Section 5.

2. Observations

2.1. SAAMER-OS: Hardware and operation overview

The Southern Argentina Agile Meteor Radar Orbital System (SAAMER-OS) is a VHF all-sky meteor orbit radar located at 53°45′8″S; 67°45′5″W hosted by the Estacion Astronomica Rio Grande (EARG) in Rio Grande, Tierra del Fuego, Argentina. Here we provide a brief overview of SAAMER-OS but we refer the reader to Janches et al. (2015) and Fritts et al. (2010) for a more in-depth description of the system and data reduction. SAAMER-OS is a SKiYMET system (Hocking et al., 1997), which started recording meteoroid orbits in January 2012, then comprising a main site (SAAMER-C) and two remote receiving stations; a northern station (SAAMER-N) at 13 km northwest of the central station; and SAAMER-W, a remote station roughly 8 km southwest of SAAMER-C.

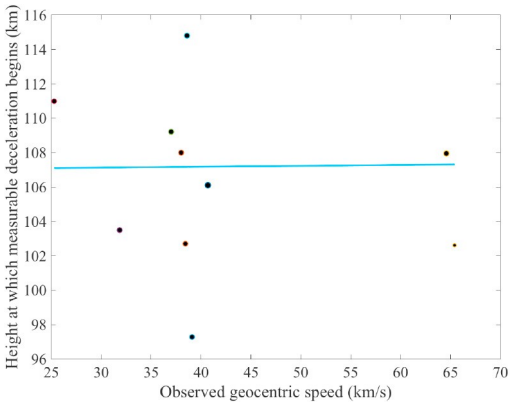

Fig. 7. Plot of estimated heights at which deceleration begins as measured with SAAMER-OS with linear fit (solid line). Data points sizes are represented as the logarithm of the number of observations.

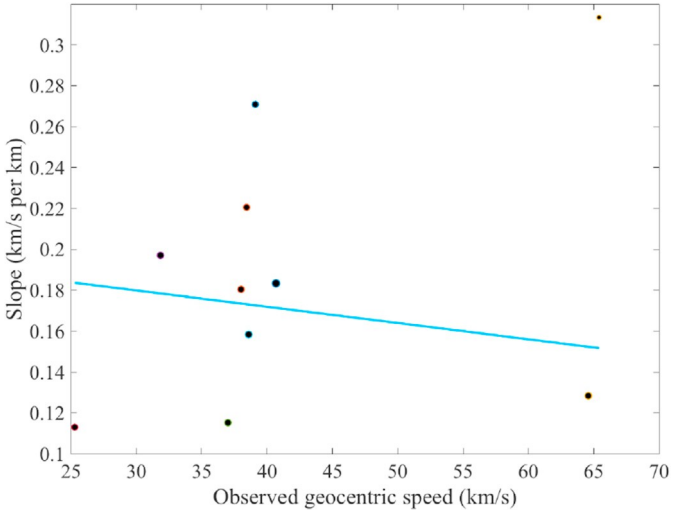

Fig. 8. Slope vs speed plot of the change in deceleration measured for the showers in Table 1 with linear fit (solid line).

Table 1
Showers used to derive the meteoroid speed correction with SAAMER-OS including fit coefficients, the number of meteors used n, and geocentric speed v_g of showers in km s^{-1}. The last three columns to the right list observed, cor- rected and reference geocentric speeds respectively.

IAU	Fit Coeff.	n	v_g		
			Obs.	Corr.	Ref.
SDA	0.1833	7906	37.7	40.8	40.7
ETA	0.1284	4160	63.4	65.0	64.6
SZC	0.1584	3548	34.2	37.5	37.7
OCE	0.1153	3250	34.7	37.7	37.0
DSX	0.1971	2906	29.3	32.1	31.3
MIC	0.1804	2671	34.2	37.8	38.0
NZC	0.2206	1969	35.7	37.8	37.5
ARI	0.2707	1710	37.7	40.3	39.1
XSA	0.1130	1511	23.2	25.9	25.3
ORI	0.3135	231	64.3	65.4	65.4

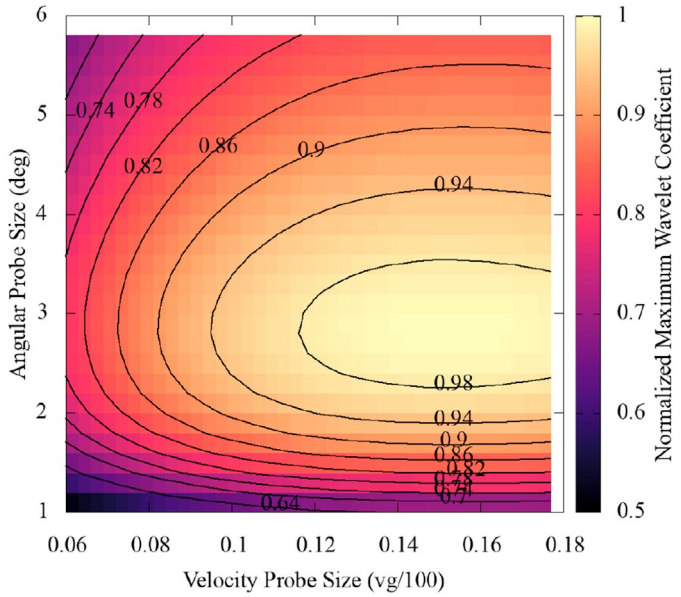

Fig. 9. Contour plot of SDA normalized maximum wavelet coefficient as a function of probe sizes at λ_0 ¼ 125° with SAAMER-OS radar detections.

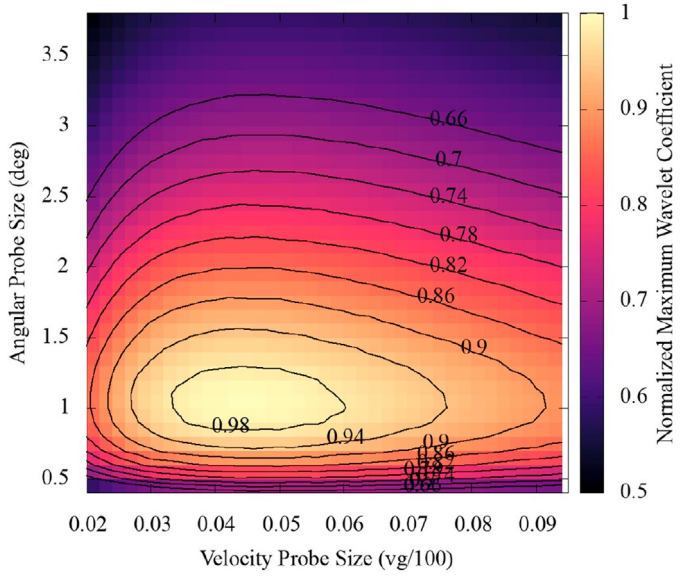

Fig. 10. Contour plot of SDA normalized maximum wavelet coefficient as a function of probe sizes at λ_0 ¼ 127° for CAMS detected meteors.

Early in 2017, a third remote station (SAAMER-S) was added to SAAMER-OS roughly 7 km south of SAAMER-C. More recently, a fourth remote station, SAAMER-E located 4 km northeast of the central station became operational in September 2019. SAAMER-C hosts the 3 wavelength-diameter circular arrangement of eight three-element crossed yagi transmitting antennas and the five-antenna three-element crossed yagi interferometer (Hocking et al., 1997; Jones et al., 1998) enabling interferometric errors less than 0.5°. With a peak transmitting power of 64 kW, SAAMER-OS employs a 7-bit Barker code to achieve 1.5 km resolution trasmiting at 32.55 MHz with opposite phasing of every other yagi, radiating the majority of the power into an all-sky gain pattern of eight 30°-wide lobes at 45° azimuth increments with peak power ~30° off zenith. This results in most of the meteor detected at off-zenith angles between 15° and 50°(Fritts et al., 2010). SAAMER-OS is uniquely agile in the sense that phases of the

Table 2
Summary of meteor showers included in our wavelet-based search methodology. λ_{max} is the time of occurrence of peak activity in solar longitude, λ_{beg} and λ_{end} are the beginning and ending dates of activity, respectively, and Dur. the total duration of the shower in degrees of solar longitude. The strength of the shower, relative to the annual background, is estimated by σ_W that is the number of standard deviations σ that the wavelet coefficient W is above the yearly median. Included are the geocentric sun-centered ecliptic and equatorial radiants along with their drift with solar longitude: $\lambda_g - \lambda_\odot$, β_g, α_g and δ_g.

IAU	SAAMER-OS			CAMS																					
	λ_{max}	λ_{beg}	λ_{end}	Dur.	σ_W	$\lambda_g - \lambda_\odot$	β_g	α_g	δ_g	α_{-g}	δ_{-g}	$\lambda_g - \lambda_\odot$	β_g	v_g	λ_{max}	λ_{beg}	λ_{end}	Dur.	σ_W	$\lambda_g - \lambda_\odot$	β_g	α_g	δ_g	α_{-g}	δ_{-g}	$\lambda_g - \lambda_\odot$	β_g	v_g
ETA	45	32	77	46	150.9	294.61	6.9	338.57	−1.57	0.69	0.35	−0.22	−0.06	65.0	46	36	86	51	253.2	293.49	7.8	338.13	−0.78	0.71	0.38	−0.19	−0.08	65.7
ARI	78	63	97	35	77.3	331.57	6.8	45.11	24.162	0.68	0.17	−0.35	−0.003	40.3	77	70	98	29	51.8	331.29	7.3	43.62	24.28	0.86	0.24	−0.19	−0.04	41.4
SZC	79	75	82	8	128.8	219.94	−14.0	304.51	−34.04	0.34	0.46	−0.61	0.38	37.5	81	76	85	10	28.1	218.29	−13.0	304.63	−32.99	0.73	0.002	−0.40	−0.13	36.1
SOP	84	62	96	35	44.6	187.26	−6.7	271.45	−30.13	0.87	−0.08	−0.24	−0.06	26.9	85	73	94	22	38.9	187.35	−5.9	272.68	−29.32	0.85	0.09	−0.24	0.08	25.4
MIC	104	84	114	31	57.2	208.52	−13.1	319.19	−29.57	0.89	0.28	−0.18	0.05	37.8	104	83	118	36	32.1	209.07	−11.0	319.03	−27.41	0.97	0.23	−0.1	−0.02	39.2
NZC	108	75	124	50	25.6	209.03	13	315.58	−3.31	0.88	0.28	−0.15	−0.04	37.8	108	71	134	64	60.6	208.92	12.7	315.56	−3.63	0.97	0.23	−0.09	0.03	38.2
SDA	125	112	155	44	300.3	209.49	−7.90	339.36	−17.20	0.79	0.26	−0.19	−0.06	40.8	127	117	175	59	317.9	208.57	−7.4	340.20	−16.34	0.84	0.34	−0.1	−0.01	40.6
CAP	125	102	134	33	47.8	178.93	9.7	303.94	−9.83	0.67	0.23	−0.31	0.1	23.7	127	97	146	50	182.5	178.73	9.8	305.67	−9.33	0.61	0.26	−0.36	0.13	22.3
NDA	142	135	158	24	20.5	207.86	7.1	347.90	2.517	0.75	0.26	−0.21	−0.006	37.7	142	134	172	39	42.8	207.66	7.1	347.71	2.44	0.77	0.34	−0.16	0.006	38.7
DSX	187	172	205	34	106.8	329.43	−11.6	153.93	−1.65	0.47	−0.54	−0.35	−0.34	32.1	191	184	193	10	40.8	329.66	−12.1	157.59	−3.64	0.69	−0.45	−0.17	−0.16	32.8
STA	197	165	232	67	21.2	194.73	−4.5	31.14	7.85	0.81	0.27	−0.16	−0.02	28.5	205	178	224	45	109.9	194.83	−4.5	38.87	10.48	0.81	0.25	−0.16	−0.02	28.2
OLP	199	190	205	16	19.0	235.8	−39.9	77.87	−17.10	0.88	0.50	0.18	0.39	27.5	201	196	202	7	14.5	239.7	−42.0	82.72	−18.80	0.83	−0.50	−0.01	−0.56	25
ORI	208	200	222	23	27.0	245.98	−7.9	94.09	15.48	0.88	0.01	−0.14	0.05	65.4	208	177	248	72	455.2	246.78	−7.7	94.92	15.66	0.77	0.05	−0.25	0.1	66.1
MCB	239	232	242	11	14.6	216.41	−45.5	94.09	−22.14	0.60	−0.10	−0.20	−0.08	43.0	243	242	254	13	14.3	214.09	−40.6	95.63	−17.30	0.93	0.49	0.09	0.57	43.4
NOO	247	227	252	16	39.7	204.20	−8.3	91.23	15.13	0.80	0.006	−0.22	−0.02	42.6	247	227	254	28	120.5	203.78	−7.9	90.81	15.54	0.77	−0.02	−0.25	−0.04	42.6
EVE	251	225	271	47	38.2	271.66	−61.3	133.67	−48.40	0.39	−0.36	−0.01	−0.14	41.3	250	237	261	25	106.5	267.22	−61	130.68	−46.70	0.79	−0.40	0.4	−0.06	41.7
SSE	274	270	290	21	31.9	327.02	17.8	242.49	−2.92	0.84	−0.19	−0.09	−0.04	42.9	272	252	288	37	13.5	328.85	15.7	241.93	−4.94	0.91	−0.24	−0.01	−0.04	43.6
VOL	280	277	283	7	22	304.1	−77.7	121.2	−72.82	0.074	−0.25	1.5	0.18	30.2	280	279	283	2	38.3	300.71	−77.6	122.05	−72.14	−2.26	−0.700	3.4	−0.3	29.3
AHY	284	272	298	27	29.8	208.5	−26.5	127.68	−8.45	0.59	−0.23	−0.3	−0.06	43.5	281	266	303	38	40.9	208.41	−26.7	127.16	−8.51	0.63	−0.12	−0.3	0.05	43.6
AAN	313	304	337	34	49.8	214.1	−19	160.67	−12.40	0.62	−0.29	−0.3	−0.02	43.6	313	296	329	34	28.7	211.27	−17	158.96	−9.51	0.77	−0.40	−0.1	−0.08	45.1

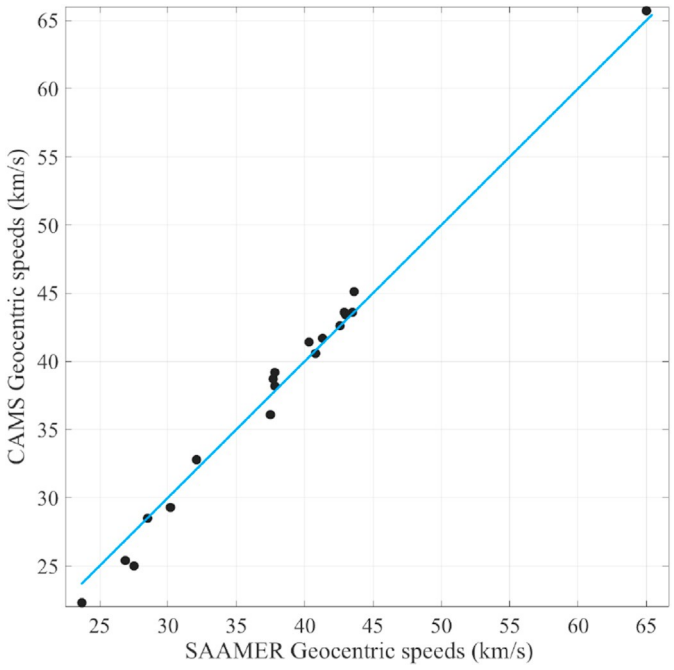

Fig. 11. Scatter plot of the wavelet geocentric speeds detected with CAMS and SAAMER-OS.

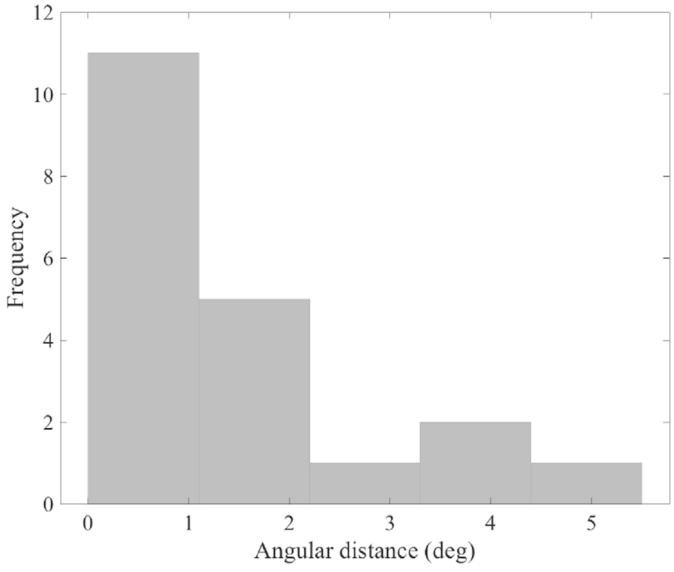

Fig. 12. Histogram of angular distances of shower radiants detected with CAMS and SAAMER-OS.

transmitting antennas are easily modified to transmit different radiation patterns as required for additional radar experiments such as head echo observations (Janches et al., 2014). SAAMER-OS employs SKiYMET's meteor echo detection and analysis algorithms developed by Hocking et al. (2001) to select specular echos from underdense meteor trains. The remote receiving stations listen to the forward-scattered pulses from an incoming meteor train a few km in length (Kaiser and Singer, 1956) and the time delays between the detection at different sites enables the determination of the in-atmosphere time-of-flight (TOF) meteoroid speed and its trajectory. This ultimately translates into the determination of the meteoroid orbital elements with this system (Janches et al., 2015; Pokorný et al., 2017). We note that previous meteor shower studies with SAAMER-OS lacked a meteoroid deceleration correction making the comparison of meteor shower orbital elements with other surveys inaccurate (Pokorný et al., 2017). Therefore we develop a meteoroid deceleration correction for SAAMER-OS in an attempt to better estimate the true out-of-atmosphere speed distribution and perform a more adequate comparison between survey results.

The peak transmitting power of SAAMER-OS exceeds those of most all-sky meteor radars typically in the 6–20 kW range, thus setting its limiting radio magnitude close to +9.5, equivalent to meteoroids down to 10^{-8} kg (or 300 μm in diameter) at 30 km s^{-1} (Verniani, 1973). Thus SAAMER-OS is likely sensitive to meteoroids an order of magnitude smaller than those detected with CMOR with a radio magnitude of +8.0 while operating at 6 kW and 29.85 MHz (Brown et al., 2008). Hardware upgrades and reduced gaps in SAAMER-OS operation translated in a steady increase in the number of meteoroid orbits recorded each year with over 350,000 in 2012 to roughly 2 million in 2018. SAAMER-OS is currently being updated to compute error estimates on radiant position and TOF speed solutions for individual meteors. Although the theoretical mean error in radiant direction for the interferometer would be less than 0.3° for meteors with elevations greater than 30°, measured errors of 1.5° or 3.0° are common for this interferometric design (Jones et al., 1998; Brown et al., 2010). For CMOR, errors are reported to be close to 1° for a subset of simultaneous optical and high signal-to-noise ratio (SNR) radar observations (Weryk and Brown, 2012). The mean spread in TOF speeds for 11 meteor showers recorded with SAAMER-OS is close to 8.5% and is similar to the median error in individual meteor speeds of 9% found in head echo -mode observations (Janches et al., 2014). We note however that for our analysis of shower orbits, the error in the mean speed is naturally smaller than for individual meteors. For this study, the SAAMER-OS database comprises meteors with valid heliocentric orbits and with SNR > 3. In Section 3.3 we describe the uncertainty estimation in shower radiant position and speeds for our wavelet-based analysis.

In this study we present eight years of continuous patrolling with SAAMER-OS resulting in 5.7×10^6 meteoroid orbits. The dataset comprises observations from 2012 through early 2019 and represents the most extensive collection of observations of sub mm-sized meteoroids in Austral latitudes to date (Galligan and Baggaley, 2004, 2005).

2.2. CAMS: Hardware and operation overview

The Cameras for Meteor Surveilance (CAMS) project comprises a number of networks that deploy numerous low-light video security cameras that measure the orbit of mm and cm-size meteoroids by triangulation of the meteor trajectory as seen against the star background. Each network consists of 3–90 cameras, spread over 2 or more locations 40–110 km apart. The cameras have a +5.4 star limiting magnitude and detect meteors of +4 to −3 magnitude, in size just above the magnitude range where sporadic meteors dominate. CAMS was designed as a validation tool for the confirmation of weak meteor showers detected in the photographic domain Jenniskens (2006).

Hardware, operations and reduction of CAMS data has been described in detail in Jenniskens et al. (2011). Each CAMS station comprises indoor computers controlling image acquisition and processing with an outdoor weather-sealed box housing the camera array. In some networks, the cameras are distributed in small numbers among many locations. In others, each CAMS station comprises of a battery of 16–20 low light-level Watec Wat902H2 Ultimate video cameras with 12-mm f/1.2 optics, each with a 30° × 22° field-of-view (FOV), plus a zenith camera affixed with a 8-mm f/1.4 lens (45° × 33° FOV), providing together a full-sky coverage above 30° elevation. Interlaced video is recorded at 60 frames per second (FPS) at 640 × 480 pixel resolution resulting in a plate scale of 2.8 arcmin pix^{-1}.

CAMS employs newly designed algorithms based on the MeteorScan software suite for daily video acquisition, calibration, meteor detection and multi-station orbit solutions, optimized to handle numerous cameras per station (Gural, 1995, 1997, 2012). CAMS incorporates a deceleration correction as part of its reduction pipeline based on empirical equations

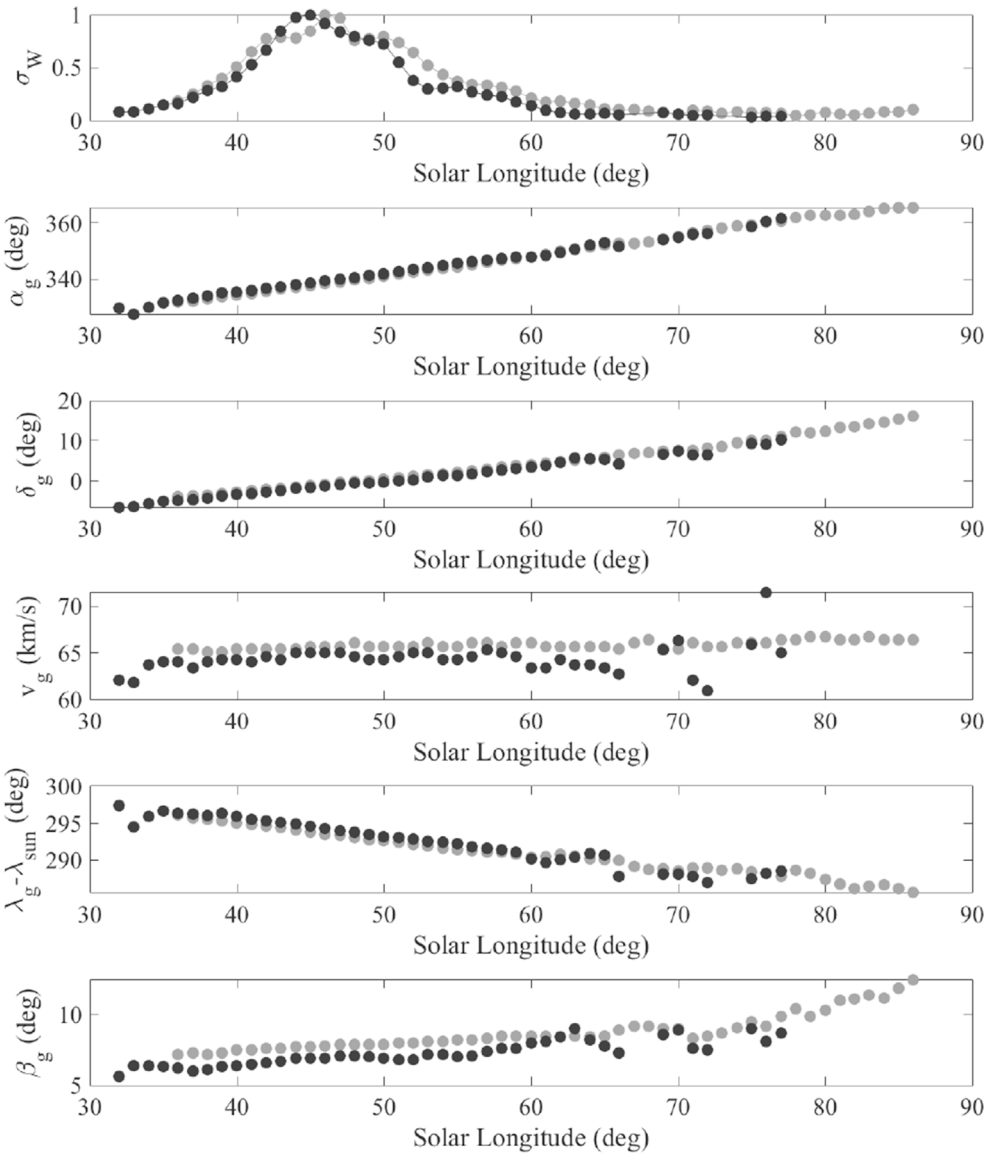

Fig. 13. Geocentric equatorial radiant chain from our linking procedure for the ETA as detected with CAMS (grey dots) and SAAMER-OS (black dots) illustrating the progression of geocentric speed v_g, geocentric equatorial coordinates δ, R.A. and normalized σ_W with solar longitude λ_0.

reported by Whipple and Jacchia (1957) and Jacchia and Whipple (1961). Until 2017, all triangulated solutions were visually inspected based on light curve shape, and linearity of the meteor trajectory in height versus range and longitude versus latitude (Jenniskens et al., 2011).

By design, CAMS excels in autonomous operation and scalability, where smaller single-CAMS amateur-run stations are added regularly to the network. The first 60-camera network was established in California in 2010. Since 2013, there are now also networks in Arizona (lead N. Moskovitz), Arkansas (lead L. Juneau), Maryland (lead P. Gural), and Florida (lead A. Howell), along with networks overseas in the BeNeLux (lead C. Johannink), New Zealand (lead J. Baggaley), and the United Arab Emirates (lead M. Odeh). BeNeLux is a distributed network among many amateur astronomers. The initial two stations in New Zealand (more recently expanded to three) are on the South Island, at Geraldine and at West Melton (Jenniskens et al., 2016b; a, 2018). The United Arab Emirate network is called the UAE Astromical Camera Network and is operated by the International Astronomical Center in Abu Dhabi. Since the majority of CAMS stations are located north of the Equator, more meteors are recorded north of the ecliptic whereas roughly 31% meteors have $\beta < 0$ (where β denotes the ecliptic latitude of the meteoroid radiant). In this study we analyze the entire CAMS dataset gathered in the years 2011–2017 that were reduced and quality controlled by visual inspection of the results. The dataset comprises of 471,582 high-resolution optical meteoroid orbits (Jenniskens et al., 2016b, a).

3. Results

3.1. Meteoroid radiant distributions

Figs. 1 and 2 show the distribution of the 471,582 optical meteoroid radiants observed with CAMS and over 5.[illegible] 10^6 meteor radiants with SAAMER-OS respectively. Figures are displayed in the usual sun-centered geocentric ecliptic frame of reference, at the center (λ_g-λ_0 270°, β_g = 0°) is the Apex of Earth's motion. Individual CAMS meteoroid radiants are color-coded by computing a radiant density as the number of adjacent radiants within 1.0° of any given radiant. Similarly, a distance of 2.8° is used to color code SAAMER-OS meteoroid radiants. This allows to enhance intrinsic features in radiant structure. The angular distances used are a proxy for the characteristic size of radiant clusters and were

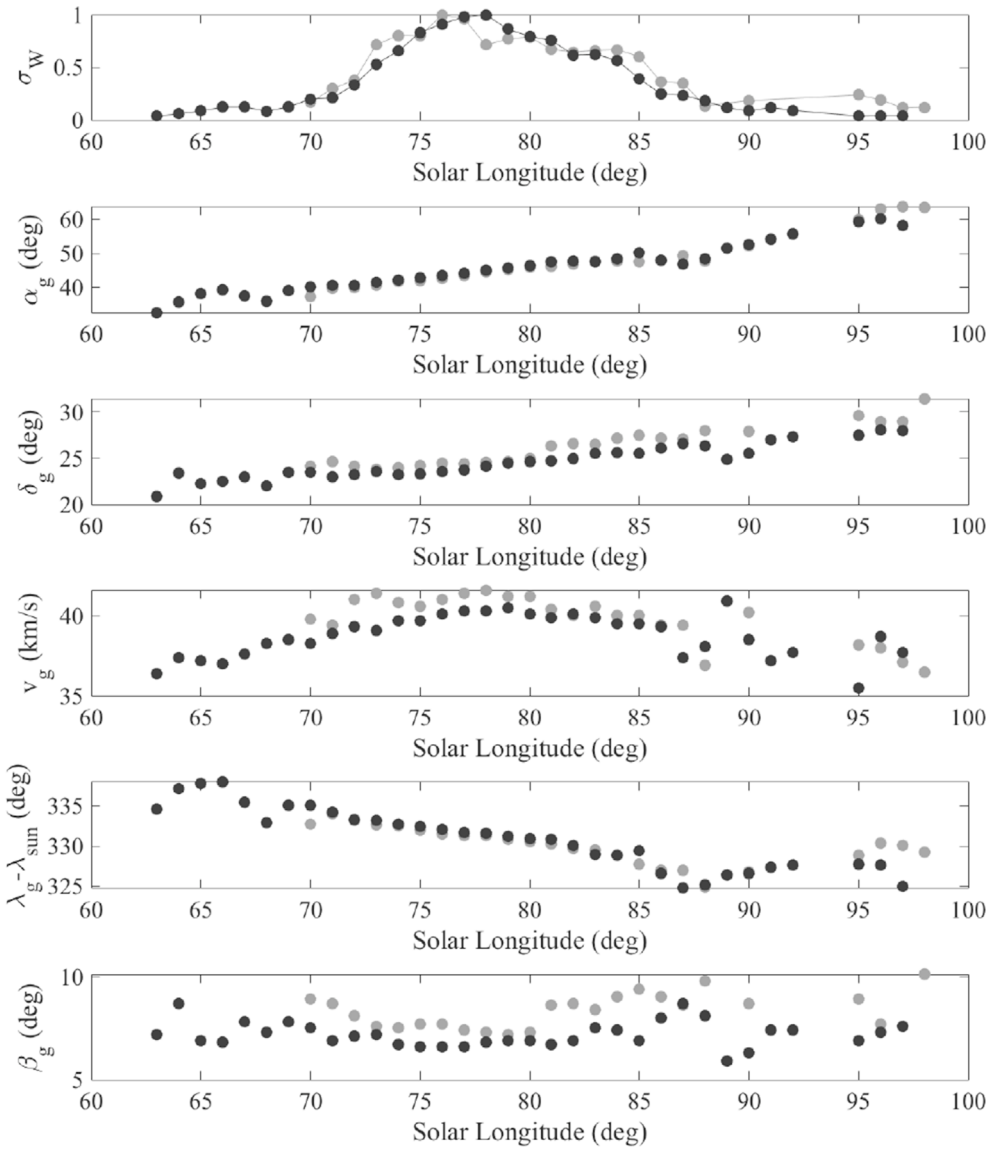

Fig. 14. ARI wavelet geocentric radiants as detected with CAMS (grey dots) and SAAMER-OS (black dots).

derived from the wavelet analysis described in Section 3.2.

Meteoroid streams are clearly evident in Fig. 1 as clumps of radiants on top of a somewhat uniform and fainter sporadic background. In contrast, Fig. 2 distinctly shows the strong contribution of sporadic sources south of the ecliptic dominating other shower structures like the η Aquarids (ETA), the Daytime Ariedtis (ARI), the Daytime Sextantids (DSX) and the South δ Aquariids (SDA). Compared against its optical counterpart, showers seem absent specially towards the Apex in the radar data because the sporadic background dominates the overall detected flux. For example, the Orionids (ORI) along with fine features like the Orionid-tail (Jenniskens et al., 2016b) are seemingly hidden under the strong sub mm-sized meteoroid flux probed by SAAMER-OS towards the southern Apex. The level of survey completeness of CAMS clearly favors the anti-helion direction, as it is expected from an optical survey. It is also biased towards northern skies since most of the observations were performed in northern latitudes (þ37° N). On the other hand, the austral location of SAAMER-OS at (−53.8° S) in addition to an observing technique which is independent of the diurnal cycle, provides a more symmetrical and homogeneous coverage with ecliptic longitude. Fig. 3 shows the number of orbits per degree of solar longitude for both surveys. There are no gaps in coverage in the stacked datasets.

3.2. *The wavelet approach*

We employ a 3D wavelet transform analysis to isolate and characterize meteor showers in CAMS and SAAMER-OS datasets. First applied to identify shower structure in radar meteoroid data with the Advanced Meteor Orbit Radar (AMOR Baggaley et al., 1994; Galligan and Baggaley, 2002), this methodology has been successfully applied to other meteoroid radar surveys (Brown et al., 2008, 2010; Bruzzone et al., 2015; Pokorný et al., 2017; Schult et al., 2018).

The wavelet transform is well suited to isolate radiant enhancements at various scales in the space of radiant coordinates, speed and time. Meteors belonging to a specific shower naturally cluster in the radiant coordinate-speed and time domain over a characteristic scale: spread in radiant coordinates, speed and activity period. Such grouping of radiants contrast with the large-scale radiant distribution of the sparse sporadic background. Therefore, a given meteor radiant distribution can be probed with the wavelet transform to reveal enhancements at a scale of interest. As in previous radar studies, we employ the 3D Mexican hat wavelet transform over a radiant distribution $f(x; y; v_g)$ given by:

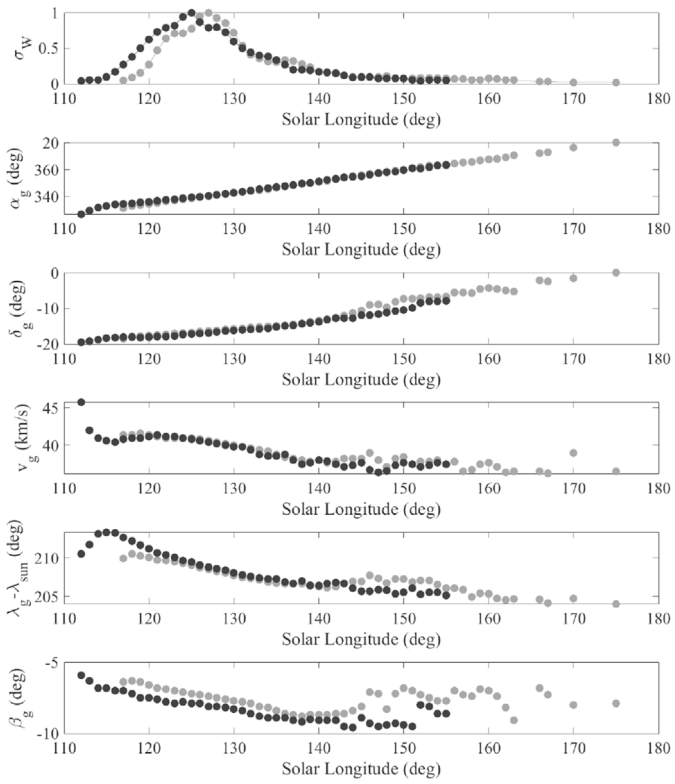

Fig. 15. SDA wavelet-based geocentric radiants detected by CAMS (grey dots) and SAAMER-OS (black dots).

$$W(x_0; y_0; v_{g0}) = \frac{1}{(2\pi)^{3/2}\sigma_v^{1/2}\sigma_a} \int_{v_{g\min}}^{v_{g\max}} \int_{-\infty}^{+\infty} \int_{-\infty}^{+\infty} f(x; y; v_g) \times \exp\left(-0.5\left(\frac{(x-x_0)^2+(y-y_0)^2}{\sigma_a^2} + \frac{(v_g-v_{g0})^2}{\sigma_v^2}\right)\right) \quad (1)$$

where $W(x_0; y_0; v_{g0})$ is the wavelet coefficient at the spatial coordinates x_0, y_0, speed v_{g0} and σ_a and σ_v are the angular and velocity probe sizes respectively. Both σ_a and σ_v control the width of the Gaussian kernel and can be adjusted accordingly to resemble the spread in angular coordinates and speed of the radiant distribution one desires to enhance.

For the radiant distribution $f(x; y; v_g)$ both the CAMS and SAAMER-OS meteor radiant datasets were separately stacked into a virtual year thus comprising all observations throughout the years 2010 through 2017 and 2012 through early 2019 respectively. The computation of Equation (1) is achieved in Sun-centered geocentric ecliptic coordinates: $x = \lambda_g - \lambda_0$, $y = \beta_g$ in degrees, geocentric speed v_g, in km s^{-1} and degrees in solar longitude. By choosing this reference frame we remove the natural motion of the sun while minimizing the radiant drift with time. Prior to our shower comparison analysis, we must correct the velocities measured by SAAMER-OS to account for the average in-atmosphere deceleration that meteoroids experience upon atmospheric entry. This correction precludes our shower wavelet-based analysis and it is a prerequisite to any meaningful comparison with other shower surveys that have been treated by similar corrections.

3.3. SAAMER-OS meteoroid deceleration correction

A major source of uncertainty in computing average meteoroid orbits is the method by which the measured velocity is converted to of the out-of-atmosphere meteoroid speed. On average, meteoroids with moderate speeds decelerate noticeably resulting in meteor echos having specular points at lower heights and lower speeds. This in turn has the effect of decreasing the average recorded meteor speed, particularly for slow-moving meteoroids, and thus affecting the estimated mean meteoroid orbital elements, especially the semi-major axis. We therefore estimate an empirical deceleration correction following Brown et al. (2004) to obtain an estimate of the true out-of-atmosphere meteoroid speed distribution.

Using the entire SAAMER-OS 2012–2019 meteor orbit dataset, we select meteors belonging to 10 meteor showers for which a reference wavelet transform-based geocentric speed is also reported in previous CMOR shower surveys (Brown et al., 2008, 2010). We employ the shower radiant position and time of peak activity reported in Pokorný et al. (2017) to compile a list of reference radiant positions for the meteor selection procedure. For the meteor extraction procedure, we use the same radiant density shown in Figs. 1 and 2. For a specific shower, we select those meteors with radiant positions inside a 10° ×10° box centered on the reported location of the shower core and within on degree around the solar longitude of peak activity. Then we compute the radiant with the maximum radiant density and use it to extract those meteors within 3° of this point.

We note that published wavelet-based speeds in Pokorný et al. (2017) are not geocentric speeds, but rather the measured TOF speeds (Pokorný, private communication, 2019). Thus we cannot use the reported shower speeds from that study. Instead, we use the shower radiant position and time of peak activity listed in Pokorný et al. (2017) and the geocentric speeds from the 2012–2019 SAAMER-OS dataset to derive the wavelet-based geocentric speed for the showers and use them to extract meteors with speeds within 20% of the computed wavelet-based geocentric speeds. Fig. 4 shows meteors within 10° × 10° from the center of the SDA meteor shower. The red cross in Fig. 4 marks the location of the core of the shower determined with the wavelet transform.

Following Brown et al. (2004), we perform a first-order fit to the distribution of meteor speeds as a function of height for each shower selected and record the height at which the linear fit matches the reference geocentric speed of the shower, the slope of the linear fit and the number of meteors utilized in the fit. The intersection height is assumed to be the height at which no deceleration have yet occurred. Repeating this procedure for each shower, a list of intersection heights, slopes, reference geocentric speeds and number of meteors is compiled. We then perform a linear fit of the slopes vs. speeds and intersection heights vs. speeds weighted on the number of meteors extracted in each shower.

Figs. 7 and 8 show the result of this procedure. Finally we combine the results derived in Figs. 7 and 8 to estimate an average deceleration factor given by:

$$\Delta v = -(-7.967 \times 10^{-4} v + 0.204) \times (h - (5.077 \times 10^{-3} v + 106.9737)) \quad (2)$$

where Δv is the difference between the observed and true speed as a function of height h (in km) and speed v (in km s^{-1}). We note that $\Delta v < 0$ in Equation (2) implies a meteor decelerating while the opposite holds for $\Delta v > 0$. In the latter case, no correction is applied. Therefore a positive correction factor of $-\Delta v$ is added to approximate the meteor true speed.

Fig. 5 shows the distribution of the correction factors estimated with Equation 2. The distribution in Fig. 5 is Gaussian-shaped with a median correction of 3:3 ± 1:1 km s^{-1} and a 95 percentile of 5.1 km s^{-1}. On average, the correction factor in not a constant offset for all meteors but rather a seemingly monotonic decreasing function with meteor height. Fig. 6 shows the average trend of the correction factor with height and on average, corrections are greater at lower speeds.

The number of meteors for which the deceleration correction becomes unreliable ($\Delta v > 0$) is 71101 or 1.26% of our sample. All such meteors have heights above 106 km with most between 106 and 120 km and a median speed of 39 km s^{-1}.

Table 1 lists the showers used to derive Equation (2) including fitting

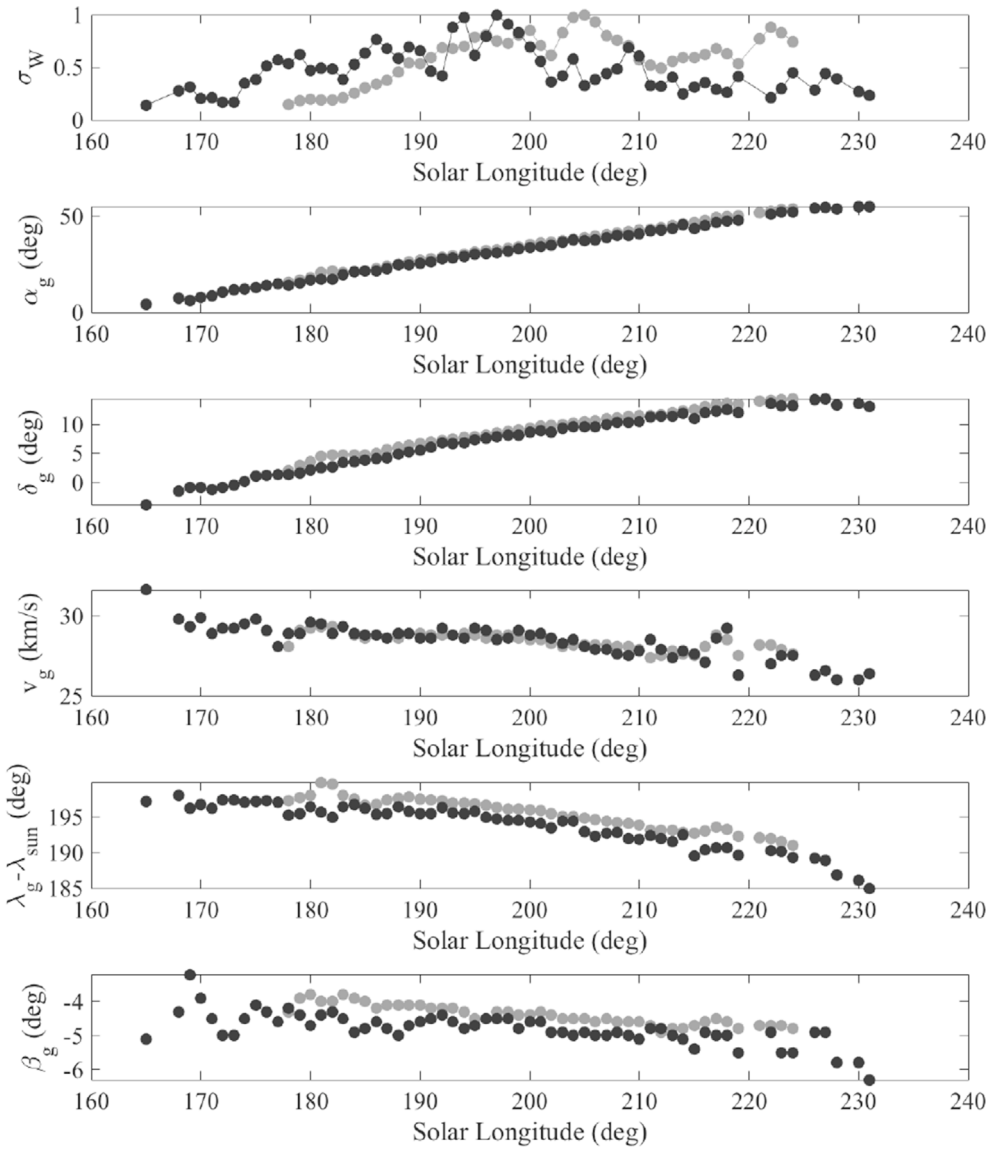

Fig. 16. CAMS (grey dots) and SAAMER-OS (black dots) detected STA geocentric radiants from the wavelet-based linking procedure.

coefficients, number of meteors used, wavelet-based speeds before and after applying Equation (2) and reference speeds. Overall, the correction results in good agreement between the speeds of showers observed with SAAMER-OS and CMOR with an average difference of 0.45 km s^{-1}. As noted in Brown et al. (2004), we find that the correction factor decreases with increasing speed. However, we also note that after applying Equation (2), most showers observed with SAAMER-OS result in speeds greater than those observed with CMOR. This is particularly noticeable for the Daytime Arietids (ARI) where the corrected speed exceeds the reference value by 1.2 km s^{-1}. We expand our discussion of the deceleration correction and elaborate on its validation in Section 4.1. We adopt the deceleration correction in Equation (2) and apply it to the entire SAAMER-OS meteor dataset.

3.4. Optimum probe sizes and shower search methodology

We first conduct a search for the scale parameters σ_a, σ_v that would maximize W in order to optimize our shower detection and characterization procedure. Following Bruzzone et al. (2015), we use this optimization on both CAMS and SAAMER-OS datasets using the Southern Delta Aquarids (SDA) meteor shower. Equation (1) is applied to all meteors in a 10° × 10° region centered at the established radiant position of the SDA given by $\lambda_g - \lambda_0$ 2 ½205 : 215] and β_g 2½ − 13 : − 3]. For the CAMS detected meteors, we center the computation to the reference geocentric speed of the SDA at v_g ¼ 41:3 kms^{-1} and date of peak activity λ_0 128° 1°(Jenniskens et al., 2016b). Similarly, for SAAMER-OS meteors we adopt the same range in coordinate space but centered at a somewhat lower geocentric speed equal to v_g ¼ 40.8 kms^{-1} since this value yielded a global maxima in W at λ_0 ¼ 125° ± 1°. We consider σ_a 2 ½; 6]degrees at 0.2° steps and σ_v 02½18 % a] 0:03% steps.

Fig. 9 and Fig. 10 show the results for the optimum set of probe sizes resulting in σ_a½2:8° and σ_v ¼5:3% as the optimum set for SAAMER-OS and σ_a¼1° and σ_v ¼4% for CAMS. The optimum probe sizes for SAAMER-OS are in agreement with those previously reported by Pokorný et al. (2017) resulting in σ_a½2:5° and σ_v ¼5% using only four years of observations and based on non corrected TOF speeds. The optimum probe size values for CAMS meteors are smaller, which is expected due to the greater resolution of optical measurements. We adopt these sets of optimum probe sizes as default parameters in our wavelet transform-based search. We note however, that other showers would have different set of optimum probe sizes, as such values relate to their intrinsic radiant structure. In Section 4.2 we elaborate further on the selection of the optimum probe sizes.

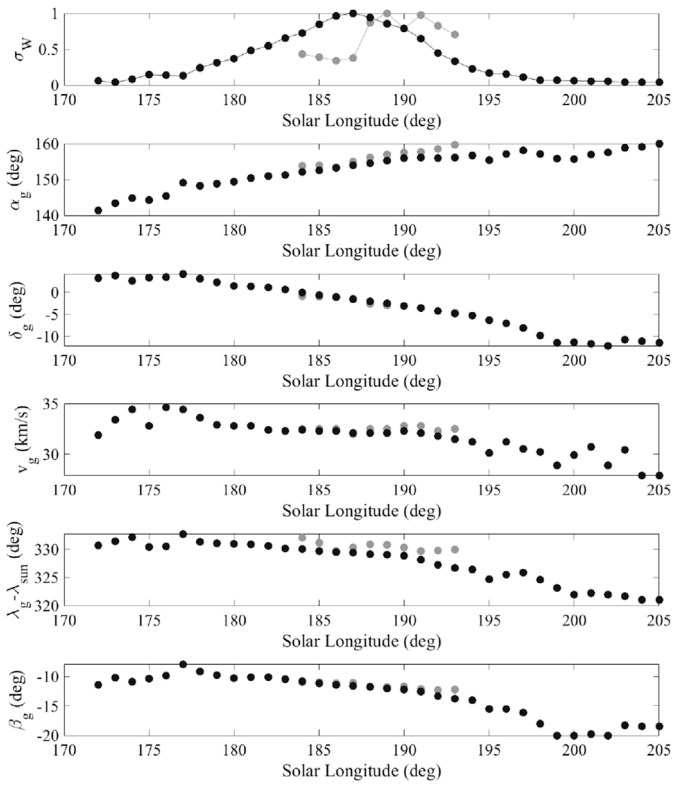

Fig. 17. CAMS (grey dots) and SAAMER-OS (black dots) detected DSX geocentric radiants from the wavelet-based linking procedure.

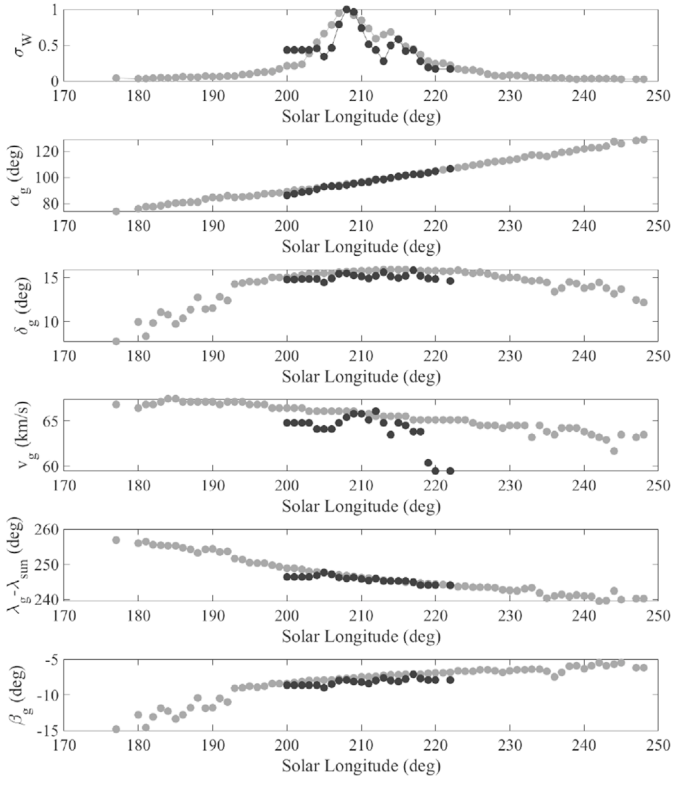

Fig. 18. CAMS (grey dots) and SAAMER-OS (black dots) detected ORI geocentric radiants from the wavelet-based linking procedure.

Following Brown et al. (2010), we apply Equation (1) to the radiant distributions in the space of Sun-centered geocentric ecliptic coordinates and geocentric speed: $\{\delta\lambda_g - \lambda_0; \beta_g; v_g\}$ binned in 1° in solar longitude λ_0. We note that evaluating Equation (1) at any given $\{\delta\lambda_g - \lambda_0; \beta_g; v_g\}$ and step in λ_0 incorporate radiants within $\lambda \mp 1{:}0°$ and those within $\pm\sigma_a$ and $\pm\sigma_v$ contribute mostly to W. We store the number of meteors in each evaluation of W in our analysis. To reduce computation costs, for each evaluation of Equation (1) we exclude meteors beyond $4\sigma_a$ in spatial coordinates and consider only those meteors with v_g within $4\sigma_v$. The evaluation of Equation (1) is CPU intensive when applied recursively at fine steps on large datasets leading to excessively large computation times. However, the recursive evaluation can be spread in parallel workloads with OpenMP and resulting times are greatly reduced.

Equation (1) is evaluated at 0:1° steps in spatial coordinates and 0:5% steps in v_g binned in 1° in λ_0 throughout the virtual year. This procedure returns a list of wavelet coefficients from which a yearly median and standard deviation σ is computed whereby a 3σ rejection is applied to remove outliers in the median computation. For those wavelet coefficients greater than 3 times the standard deviation above the median the local maximum is stored and a list of wavelet maxima created. We proceed to identify a shower core radiant in geocentric sun-centered ecliptic coordinates and speed: $\{\overline{\delta\lambda_g} - \overline{\lambda_0}; \overline{\beta_g}; \overline{v_g}; \overline{\lambda_0}\}$ as the radiant producing the wavelet coefficient global maxima.

Once the shower core location is identified, we create a chain of linked radiants through time that yield wavelet coefficient maxima. Similarly by Pokorný et al. (2017), we consider radiants linked if they are less then 3° apart, have speeds up to 15% of the shower core speed and no more than 3° in solar longitude apart. The linking procedure also requires that linked radiants follow a consistent linear trend in geocentric equatorial coordinates: α_g and δ_g with time. For each shower, we perform a linear fit in α_g, δ_g, λ_g–λ_0 and β_g with solar longitude and used them as measure of the shower drift in those coordinates.

3.5. Uncertainties in radiant position and speeds from the wavelet analysis

The accuracy of the daily shower radiant positions from our wavelet-based analysis can be approximately estimated by comparing them to the measured position of the core of the showers. We use the difference between the observed radiant distribution and the returned values from the wavelet analysis as a proxy for the uncertainty in the individual mean position of the showers.

We follow a similar procedure to extract shower meteors as outlined in Section 3.3. The observed shower core position is estimated as the radiant position with the maximum radiant density as calculated for Figs. 1 and 2. We use the newly computed shower core positions and speeds from our wavelet analysis and select meteors with speeds within 15% and 4% of the wavelet-based speeds for SAAMER-OS and CAMS observations respectively.

To estimate the uncertainty in the individual shower speed, we compute the standard error of the mean meteor speed extracted for each shower. We apply this procedure repeated to the 20 showers studied in this work. The result is an average radiant position uncertainty of 0.60° and 0.63° with average speed uncertainties of 0.24 km s^{-1} and 0.03 km s^{-1} for SAAMER-OS and CAMS observations respectively.

3.6. Shower results

In this section we summarize the search results for the 20 established showers selected in this study. We refer the reader to the Supplementary Material available online for additional data and figures resulting from the wavelet search methodology.

Table 2 lists the meteor showers included in this study. The deceleration correction bridged the gap between the wavelet-based geocentric speeds from both surveys with a median difference of 0.7 km s^{-1}. We find that 12 out of 18 (67%) showers have a difference in speed below 1.1 km

Table 3
Orbital elements for the showers in our wavelet-based analysis observed with SAAMER-OS and CAMS. Shower orbital elements are derived with the wavelet-based geocentric radiant at the time of peak activity, N is the number of meteors contributing to W and T_J is the Tisserand parameter.

IAU Code		λ_{max}	a	e	i	ω	Ω	M	q	T_J	N
ETA	SAAMER-OS	45	7± 2	0.93 ± 0.01	165.4 ± 0.9	92 ± 1	45	1.9 ± 0.6	0.54 ± 0.01	−0.08	2825
	CAMS	46	9.1 ± 0.2	0.937 ± 0.001	163.8 ± 0.1	96.9 ± 0.1	46	1.44 ± 0.04	0.579 ± 0.001	−0.3	675
ARI	SAAMER-OS	78	2.3 ± 0.1	0.967 ± 0.002	25 ± 1	27.9 ± 0.7	78	9.7 ± 0.6	0.075 ± 0.003	2.6	1230
	CAMS	77	2.6 ± 0.2	0.973 ± 0.001	29 ± 2	28 ± 1	77	7.6 ± 0.7	0.071 ± 0.005	2.3	34
SZC	SAAMER-OS	79	1.05 ± 0.01	0.932± 0.003	56 ± 1	157.9 ± 0.6	259	325.7 ± 0.8	0.072 ± 0.003	5.1	4600
	CAMS	81	1.03 ± 0.01	0.930 ± 0.002	47.3 ± 0.8	158.0 ± 0.5	261	324.2 ± 0.6	0.073 ± 0.002	5.3	34
SOP	SAAMER-OS	84	2.36 ± 0.06	0.817 ± 0.004	6.9 ± 0.2	106.2 ± 0.5	264	347.8 ± 0.5	0.432 ± 0.003	3.0	2609
	CAMS	85	1.9669	0.77349	5.8267	106.6958	265	343.2824 ± 0.0006	0.44553	3.4	216
MIC	SAAMER-OS	104	1.84 ± 0.07	0.932 ± 0.002	37 ± 1	145 ± 1	284	345.6 ± 0.9	0.126 ± 0.006	3.2	3240
	CAMS	104	2.0 ± 0.1	0.951 ± 0.002	36 ± 2	48 ± 1	284	348.0 ± 0.9	0.010 ± 0.007	2.9	81
NZC	SAAMER-OS	108	1.730 ± 0.09	0.931 ± 0.003	36 ± 2	326 ± 1	108	344 ± 1	0.120 ± 0.008	3.3	2781
	CAMS	108	1.81 ± 0.08	0.935 ± 0.002	36 ± 2	326 ± 1	108	345 ± 1.0	0.117 ± 0.007	3.2	161
SDA	SAAMER-OS	125	2.41 ± 0.04	0.9706 ± 0.0005	31.5 ± 0.5	152.7 ± 0.3	305	351.2 ± 0.2	0.071 ± 0.001	2.4	11448
	CAMS	127	2.50 ± 0.03	0.9695 ± 0.0002	28.3 ± 0.4	151.5 ± 0.2	307	351.7 ± 0.1	0.0763 ± 0.0009	2.4	1506
CAP	SAAMER-OS	125	3.0 ± 0.1	0.807 ± 0.007	7.5 ± 0.2	268.5 ± 0.4	125	351.4 ± 0.5	0.574 ± 0.003	2.6	1001
	CAMS	127	2.43 ± 0.04	0.756 ± 0.003	7.1 ± 0.2	268.2 ± 0.5	127	348.0 ± 0.3	0.592 ± 0.003	3.0	544
NDA	SAAMER-OS	142	2.0 ± 0.2	0.950 ± 0.004	21 ± 3	328 ± 2	142	348 ± 2	0.10 ± 0.01	3.0	1293
	CAMS	142	2.28 ± 0.09	0.9585 ± 0.0007	22 ± 1	328.5 ± 0.8	142	350.2 ± 0.6	0.094 ± 0.004	2.6	292
DSX	SAAMER-OS	187	1.055 ± 0.009	0.872 ± 0.002	25.8 ± 0.5	210.8 ± 0.4	7	36.7 ± 0.5	0.134 ± 0.002	5.3	2255
	CAMS	191	1.11 ± 0.02	0.878 ± 0.003	27 ± 1	211.7 ± 0.9	11	34 ± 1	0.135 ± 0.006	5.1	25
STA	SAAMER-OS	197	1.8 ± 0.1	0.82 ± 0.01	5.7 ± 0.5	120.3 ± 0.8	17	343 ± 2	0.320 ± 0.007	3.6	1061
	CAMS	205	1.75 ± 0.06	0.820 ± 0.003	5.6 ± 0.7	120.3 ± 1	25	341 ± 1.0	0.323 ± 0.008	3.6	591
OLP	SAAMER-OS	199	0.760 ± 0.004	0.561 ± 0.002	54.9 ± 0.7	148.4 ± 0.5	19	262.9 ± 1	0.334 ± 0.003	7.2	671
	CAMS	201	0.731 ± 0.003	0.526 ± 0.005	50.1 ± 0.1	153.4 ± 0.4	21	247.8 ± 0.7	0.346 ± 0.005	7.5	7
ORI	SAAMER-OS	208	6 ± 4	0.92 ± 0.02	163.0 ± 0.6	88 ± 2	28	358 ± 5	0.54 ± 0.01	0.06	294
	CAMS	208	8.1 ± 0.4	0.930 ± 0.003	163.8 ± 0.3	83.8 ± 0.3	28	358.3 ± 0.1	0.568 ± 0.003	−0.23	2462
MCB	SAAMER-OS	239	8 ± 12	0.92 ± 0.02	68.1 ± 0.6	77 ± 1	59	358 ± 6	0.622 ± 0.007	1.0	832
	CAMS	243	8 ± 9	0.93 ± 0.01	67.3 ± 0.7	88 ± 2	63	358 ± 5	0.53 ± 0.01	1.0	35
NOO	SAAMER-OS	247	8 ± 2	0.987 ± 0.003	25.2 ± 0.8	141.6 ± 0.6	67	359 ± 4	0.113 ± 0.003	1.0	716
	CAMS	247	10 ± 1	0.989 ± 0.001	23.7 ± 0.7	141.1 ± 0.6	67	359.0 ± 0.2	0.114 ± 0.003	0.90	336
EVE	SAAMER-OS	251	2.3 ± 0.1	0.56 ± 0.03	74.3 ± 0.5	358 ± 107	71	0 ± 108	0.9855 ± 0.0004	2.6	2074
	CAMS	250	2.3 ± 0.2	0.58 ± 0.03	74.9 ± 0.5	5 ± 46	70	359 ± 47	0.985 ± 0.001	2.5	61
SSE	SAAMER-OS	274	2.1 ± 0.2	0.937 ± 0.005	59 ± 2	38 ± 2	274	11 ± 1	0.13 ± 0.01	2.7	1038
	CAMS	272	2.6 ± 0.2	0.956 ± 0.003	54 ± 2	37 ± 1	272	7.6 ± 0.8	0.117 ± 0.007	2.2	7
VOL	SAAMER-OS	280	3.1 ± 0.7	0.69 ± 0.04	49.7 ± 0.8	166.2 ± 0.7	280	1.8± 0.4	0.97 ± 0.001	2.4	503
	CAMS	280	2.6 ± 0.2	0.63 ± 0.03	48.9 ± 0.5	167 ± 1	280	2.4 ± 0.4	0.973 ± 0.002	2.7	20
AHY	SAAMER-OS	284	7 ± 2	0.968 ± 0.008	58.2 ± 0.7	116.7 ± 0.9	104	358 ± 4	0.286 ± 0.005	1.0	683
	CAMS	281	8 ± 1	0.961 ± 0.005	58.4 ± 0.6	116 ± 1.0	101	358.2 ± 0.4	0.290 ± 0.006	1.0	66
AAN	SAAMER-OS	313	2.4 ± 0.1	0.940 ± 0.003	63.3 ± 0.9	140.0 ± 0.8	133	350.6 ± 0.8	0.142 ± 0.004	2.4	1773
	CAMS	313	4.5 ± 0.5	0.971 ± 0.002	59 ± 1	140 ± 1	133	356.6 ± 0.5	0.131 ± 0.006	1.4	39

s^{-1} and only three (17%) above 1.5 km s^{-1}.

The largest difference is found for the October Leporids (OLP) at 2.5 km s^{-1}. The OLP, the β-Canis Majorids (MCB) and the σ-Serpentids (SSE) do not show a good agreement between surveys as illustrated by the lack of consistent trend in shower coordinates with time. Due to the low number of detections for these showers it is not possible at this time to determine if these differences are due to real effect or low-number statistics. Incidentally, our wavelet-based transform returns only 7 OLP and 7 SSE meteors with CAMS and thus they are not optimal for comparison and therefore excluded. Fig. 11 shows the correlation between the geocentric speeds resulting from both datasets with a correlation factor equal to 1.054.

Fig. 12 shows the distribution of the differences in shower radiant position. The median difference in shower radiant position is 0.81° with 77% of showers having a difference below 2°. The largest difference is found for the weaker β Canis Majoris (MCB) at 5.2°. The MCB is not a particularly strong shower due to its relative low σ_W 14 not showing a clear single-peaked profile in σ_W as a function of λ_0 in the CAMS observations. However, although the largest difference in shower radiant position occurs for the weak MCB with σ_W 14:3, 60% of showers have a difference in radiant position less than 1.1°. We don't find a correlation between the differences in shower speed with shower intensity as measured by σ_W. We find that 67% of showers have differences in speed less than 1.1 km s^{-1} even though σ_W is below 40.

Our wavelet analysis also returns a mean difference of 1° for the time of the shower peak activity in both surveys with 77% of showers achieving peak activity less than 2 days apart. We do not find evidence to support the assumption that weaker showers have larger differences in peak activity. We note however that for any given λ_0, the computation of W incorporates radiants at $\lambda_0 \pm 1°$ (Brown et al., 2010; Bruzzone et al., 2015; Pokorný et al., 2017; Schult et al., 2018). Figs. 13–18 show examples of our wavelet transform-based linking procedure for the η − Aquariids, the Daytime Arietids, the Southern δ − Aquariids, the Southern Taurids (STA), the Daytime Sextantids (DSX) and the Orionids for both SAAMER-OS and CAMS. For each shower, we include the evolution of equatorial geocentric radiant positions: α_g , δ_g , geocentric sun-centered ecliptic longitude and ecliptic latitude: $\lambda_g - \lambda_0$, β_g , geocentric speed, v_g and σ_W with solar longitude and use the evolution of σ_W in time as a proxy for the activity profile of showers. We note however that a proper flux computation is pending in this study and emphasize this limitation when comparing the activity profiles of showers and the interpretation of shower activity.

Table 3 summarizes the orbital elements with uncertainties derived following the procedure in Section 3.5. Shower orbits are computed with their wavelet-based ecliptic geocentric radiants at the time of peak activity. The number of meteors used to compute the orbits N is included in Table 3. To derive uncertainties in orbital elements, we employ a Monte Carlo approach based on the uncertainties in radiant position and speed for each shower. We note that in this procedure the uncertainties reflect the precision rather than an estimate of the accuracy. The agreement in orbital elements and Tisserand parameter T_J evidently follows the same trend arising from the similarities found in radiant position and

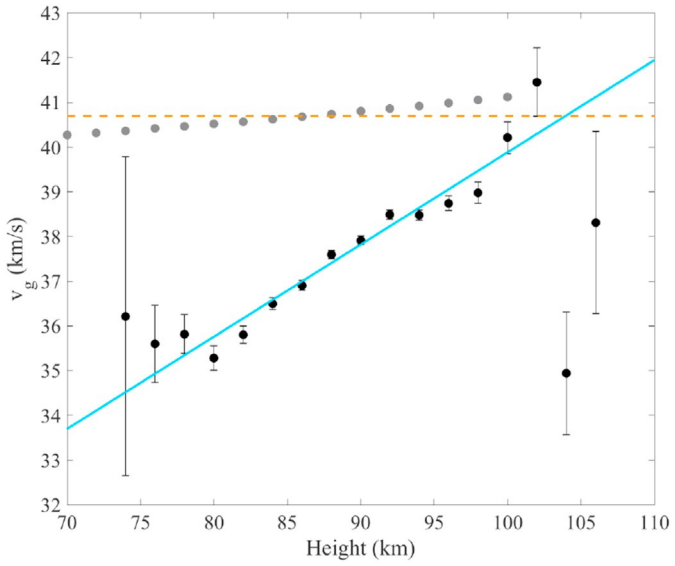

Fig. 19. SDA speed deceleration profile for meteors detected with SAAMER-OS, with linear fit (solid line) and the wavelet-based speed from this study (horizontal dashed line). Individual black data points are meteor speeds averaged in 2 km height bins with error bars representing the standard error in mean speeds. Grey dots are meteor speeds from the linear fit corrected for deceleration with Equation (2).

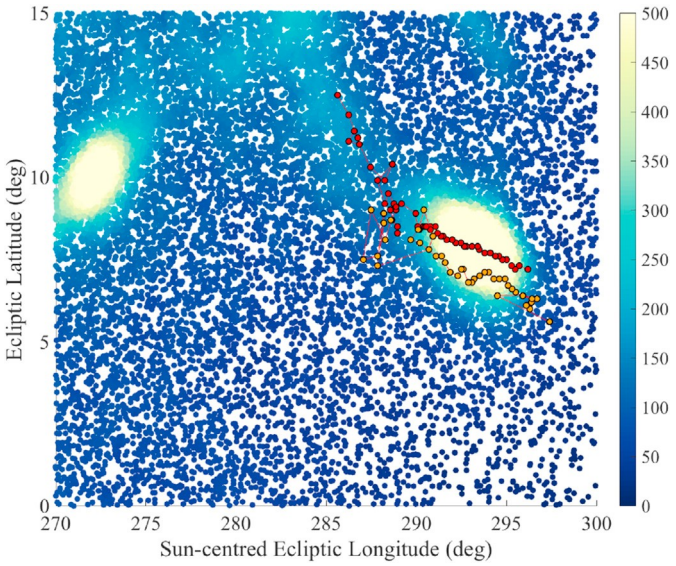

Fig. 20. ETA and λ − Geminids meteors in radiant density map of CAMS observations with linked radiants derived with the wavelet-based methodology from CAMS (red dots) and SAAMER-OS (orange dots) observations. (For interpretation of the references to color in this figure legend, the reader is referred to the Web version of this article.)

Table 4
Optimum probe sizes for five meteor showers observed with CAMS and SAAMER-OS.

IAU	SAAMER-OS			CAMS		
	v_g	σ_a	σ_v	v_g	σ_a	σ_v
	kms^{-1}	(deg)	%	kms^{-1}	(deg)	%
SDA	40.8	2.8	15.3	40.6	1.0	4.4
ETA	65.0	2.4	11.5	65.7	0.5	1.6
CAP	23.7	2.6	16.0	22.3	1.1	4.4
STA	28.5	5.4	17.5	28.5	1.9	7.6
NOO	42.6	3.2	10.5	42.6	1.2	3.3

geocentric speeds and overall, the orbital elements are in agreement to those found in the literature (Jenniskens et al., 2016b). We note however that for SAAMER-OS showers, the deceleration correction is likely a dominant source of uncertainty affecting specially v_g and the semi-major axis.

η-*Aquariids (ETA).* This shower belongs to the group of 1P/Halley streams and is the second strongest shower in SAAMER-OS placed eastward of the North Apex sporadic source. It is also the third strongest shower in the CAMS dataset with σ_W¼253:2. The speed values from our wavelet analysis are close to those from other radar and optical surveys with a max difference of 0.7 km s^{-1} (Galligan and Baggaley, 2002; Brown et al., 2008; Jenniskens et al., 2016b). The orbital elements in Table 3 are in good agreement whereas a smaller semimajor axis is estimated for radar meteoroids. Nevertheless, the smaller semimajor axis is consistent with previous radar and optical studies and within uncertainties to the estimated from the optical CAMS survey. Our analysis extends the activity period of the shower by 10° in λ_0 with radar and up to approximately 20° in the optical compared to previous surveys (Galligan and Baggaley, 2002; Brown et al., 2010; Jenniskens et al., 2016b; Pokorný et al., 2017). Fig. 13 illustrates ETA radiant chains for optical and radar meteoroids returned by our wavelet analysis with nearly identical shower core motion with time. The wavelet analysis returns almost identical non-symmetrical profiles in σ_W with a knee at $\lambda\sigma$~50° and a sudden drop followed by bump in activity approximately 5° later.

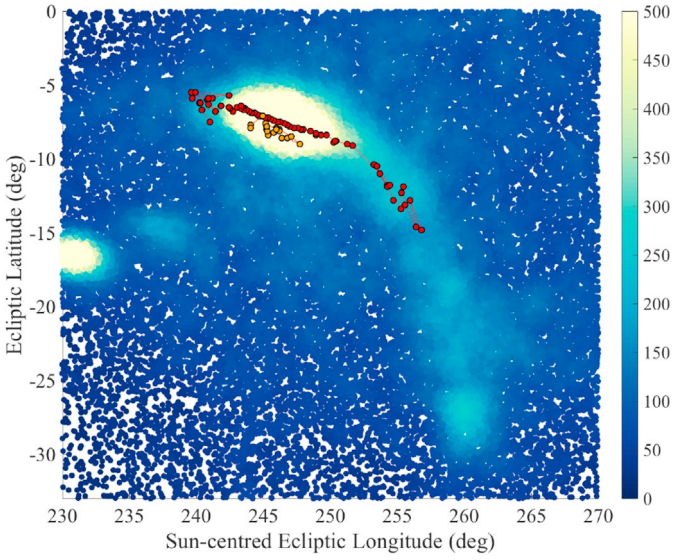

Fig. 21. CAMS radiant density map of the ORI with CAMS (red dots) and SAAMER-OS (orange dots) radiants derived with the wavelet-based methodology. (For interpretation of the references to color in this figure legend, the reader is referred to the Web version of this article.)

Daytime Arietids (ARI). Arguably one of the strongest daytime meteor showers, the Daytime Arietids are active from mid-May to late-June achieving peak fluxes over 0.035 meteoroids km^{-2}hr^{-1} (Bruzzone et al., 2015). This places the ARI above the Perseids and Geminids both in activity and duration in radar observations. On the other hand, for visual surveys it becomes difficult to measure Daytime Arietids radiants close to the Sun. For instance, the wavelet-based analysis returns only 34 video meteors with CAMS at the time of peak activity. Also known as one of the 96P/Machholz showers (Jenniskens, 2006), ARI has been associated with the Marsden group of sunskirting comets (Sekanina and Chodas, 2005; Jenniskens, 2006; Jenniskens et al., 2012). Fig. 14 shows the results from our wavelet analysis returning an extended period of activity

of this shower while reproducing its broad 10° profile (FWHM); possible suggesting an old age for the stream. However we stress that orbital elements from both surveys agree within uncertainties, specially in semimajor axis. The similarity in semimajor axis suggest a seemingly comparable young age for the population of small sub-mm size and cm-sized meteoroids, in contrast with previous radar findings using CMOR observations (Bruzzone et al., 2015). We revisit the Daytime Arietids and elaborate the discussion further in Section 4.3.

South δ-Aquariids (SDA). As shown in Fig. 15, this is clearly the strongest shower detected with SAAMER-OS (σ_W = 300:3). The SDA is another Machholz shower standing well above the sporadic background with a peak activity in late July (λ_0 = 125°). The SDA is also strong in the CAMS survey with σ_W = 318, second only to the Orionids (ORI) in integrated strength. Shower activity as seen with CAMS (peak at λ_0 = 127°) lags 2° behind the results derived with the radar before the peak. After the peak activity, however, the activity profile from both datasets agree closely. The drift in α_g, δ_g, $\lambda_g - \lambda_0$ and β_g from both surveys is almost identical up to approximately λ_0 = 140° when the radar radiants show a higher drift in δ_g. The wavelet analysis was able to identify the August *o*-Aquariids (AOA; α_g = 348:5°, δ_g = −14:4°, v_g = 38:2 km s^{-1}) in the CAMS survey for $\lambda_\odot$ = 132° (Jenniskens, 2006), as expected because the AOA were identified as a mere component of the overall SDA in the activity and radiant drift profiles (Jenniskens et al., 2016b).

Southern Taurids (STA). Part of the southern branch of the 2P/Encke stream in the Anti-Helion region, the STA is formed by several 3-10 day-long components with a combined active period between $\lambda_\odot$ = 180° and approximately $\lambda_\odot$ = 260° (Jenniskens, 2006). Fig. 16 shows the wavelet analysis on SAAMER-OS observations of the STA shower peaking at λ_0 = 171°, preceding by approximately 14° the earliest activity seen with CAMS. Despite the similarities in radiant position, speeds, and orbital elements, the SAAMER and CAMS activity profiles are distinct. Both profiles are irregular, with SAAMER rates higher at low solar longitudes, peaking 8 degrees early. We note however that, his shower suffers from bad weather during the northern hemisphere CAMS observations. We elaborate more on the wavelet analysis results of the STA in Section 4.3.

Daytime Sextantids (DSX). This shower of the Phaethon family is located south west of the Helion Source and thus well positioned for radar surveys. The wavelet analysis in Fig. 17 indicates a definite detection of this shower in SAAMER-OS observations (σ_W = 106:8) peaking at λ_0 = 188° lasting 34° of activity (FWHM = 8°). However, as with other daytime showers, only 25 DSX video meteors were used in the wavelet transform at the time of peak activity. The wavelet analysis yields a peak date 2° behind the reported dates with CMOR and AMOR but at a speed approximately 0.9 km s^{-1} higher. (Galligan and Baggaley, 2002; Brown et al., 2010). CAMS observations also detect the shower, but it rises above the horizon only in the hours before sunrise. As a result, the CAMS-detected shower has a lower σ_W = 40:8 and is active for a shorter period of time, not surprising for a daytime shower. The analysis returns an average shower speed 0.7 km s^{-1} faster in the optical, a trend observed in previous comparisons between radar and optical observations (Galligan and Baggaley, 2002; Brown et al., 2010; Jenniskens et al., 2016b). However, this trend is not significantly larger than the estimated uncertainties introduced by the deceleration correction in Section 4 preventing therefore a more meaningful interpretation.

Orionids (ORI). This second Halley-type stream is the strongest shower in the CAMS survey (σ_W = 455:2) lasting over 72° in λ_0, Fig. 18. On the other hand, this shower is rather weak in SAAMER-OS observations as evident from the low meteor count and σ_W = 27. Date of peak activity, radiant position and shower speed from SAAMER-OS agree from those reported with CMOR. Interestingly, the wavelet analysis records seemingly mirrored doubled-peaked profiles in σ_W with features reminiscent of the activity profile of the ETA steam. We continue the discussion of the activity profile of the Orionids in 4.3.

4. Discussion

Our wavelet-based analysis provides an unique method for characterizing meteor streams as probed by two different observing techniques. Results in Table 2 show a general agreement between SAAMER-OS and CAMS results with very similar radiant positions, speeds and occurrence of peak activity. The orbital elements from the resulting showers are presented in Table 3. The deceleration correction derived in Section 3.3 results in good agreement between shower speeds measured with CMOR in Tables 1 and 2.

Although SAAMER-OS uncertainties in individual meteor radiant position and speed could be as large as 3.0° and 8% respectively, our wavelet-based mean results indicate a very good agreement with shower radiants from other studies. However, although the estimated uncertainties in the mean position and speed for showers with SAAMER-OS are low, a remaining source of uncertainty pertains to the magnitude of the deceleration correction applied to individual meteor speeds.

4.1. Deceleration correction

The magnitude of the deceleration correction introduced in Equation (2) could be a dominant source of uncertainty in the estimate of the wavelet-based shower speeds with a direct effect on the resulting orbital elements. Comparing SAAMER-OS with other radar surveys we find that corrected mean geocentric shower speeds measured with SAAMER-OS and AMOR differ on average 0.56 km s^{-1}, but for two showers, the α−Capricornids (CAP) and the Daytime Sextantids, the speeds differ by 0.9 km s^{-1}. The mean shower speeds in Table 2 with SAAMER-OS differ on average by 0.4 km s^{-1} with respect to those measured with CMOR. On the other hand, the Daytime Arietids and the October Leporids are the showers where the speed difference is the largest, at 1.4 km s^{-1} and 2.0 km s^{-1} respectively.

We investigate how the deceleration correction performs on individual meteor speeds of the Southern δ-Aquariid shower. Fig. 19 illustrates the effect of the deceleration correction applied to SDA meteors. We selected SDA meteors averaging their speeds inside a 2 km-wide height bin extracted in the vicinity of the SDA core following the same selection procedure introduced in Section 3.3. This returns a deceleration profile with mean meteor speeds at 2 km steps in height with error bars indicating the standard error in mean speeds. We then perform a linear fit (solid line) weighted on the number of meteors at each height bin and apply the deceleration correction to the resulting fit (grey dots). If Equation (2) perfectly removes the speed-height correlation, we would expect the corrected profile to lie along an horizontal line in Fig. 19. The wavelet-based speed for the SDA is indicated by the horizontal dashed line. Overall, Equation (2) performs well but in may introduce differences of ~0.3–0.5 km s^{-1} in the true shower speed.

A similar result was found applying the Brown et al. (2004) correction on Daytime Arietids speeds observed with CMOR (Bruzzone et al., 2015). The authors found that ARI meteor speeds could be overcompensated by ~0.4 km s^{-1} and thus opted to incorporate an ablation model to independently estimate the true out-of-atmosphere speed leading to a shower semimajor axis estimate of 1.7±0.2 AU. On the other hand, our derived semimajor axis for the ARI of 2.3±0.1 AU is greater and in closer agreement to the value derived with CAMS and other visual reports supporting the believe that the ARI is a Machholz stream. We note that following a similar procedure used to create Fig. 19, we independently estimate an out-of-atmosphere geocentric speed of 39.7 km s^{-1} for the ARI, 0.4 km s^{-1} below the wavelet-based speed reported here. Such difference in shower speed returns a semimajor axis of 2.1 AU, still above the value reported with CMOR. Although a systematic error introduced by applying Equation (2) seems likely, the independent estimate of the shower speed with SAAMER-OS indicates that the difference in the observed speeds between surveys may be real and demands further investigation.

A more robust method for meteoroid deceleration is currently being

developed incorporating the Chemical Ablation Model (CABMOD) (Vondrak et al., 2008) to improve shower speeds and orbits with SAAMER-OS.

4.2. Selection of optimum probe sizes and radiant dispersion

The selection of the optimum probe sizes in our analysis maximized wavelet coefficient values and hence improved our retrieval of meteor shower radiants. However, since the probe sizes are a measure of the shower scale and spread in radiant space, we suspect that the derived probe sizes for the strong SDA might not be a representative sample of the meteor shower population. We therefore investigate how the optimum probe sizes vary across five showers and we compare them against the SDA. Table 4 shows the resulting optimum values for the SDA, ETA, CAP, STA and November Orionids (NOO) meteor showers.

The list of optimum probe sizes show that meteor showers detected in the optical systematically have narrower clusters in radiant position and speed. This is expected due to larger measurement errors in radar observations. Furthermore, for each shower, the probe sizes from CAMS and SAAMER-OS change in a consistent manner.

For both observing techniques, small differences in probe size values between showers could be the result of measurement precision of individual orbits or due to the different level of difficulty identifying the stream over the sporadic background.

Alternatively, some of the differences might reflect a more rapid dispersion of small meteoroids that are more prone to radiation pressure. However, Table 4 also suggest a minimum wavelet-based dispersion greater than 2° as a lower limit on radar radiant dispersion measurements with SAAMER-OS. Differences in dispersion seen by both techniques are likely related to encounter geometry and the age of the stream. For example, the large probe sizes found for CAMS and SAAMER-OS for the STA indicates significant dispersion for this stream.

We do not expect a strong negative impact in our analysis due to the variation in optimum probe size values found above. The slow variation of W with probe size values shown in Figs. 9 and 10 suggest that our analysis will not be severely affected by the adopted values in Section 3.4.

4.3. Activity profiles

The wavelet technique reveals that most showers display seemingly mirrored activity profiles as probed by the evolution in σ_W with time. The profiles in Figs. 13, 15 and 18 clearly show asymmetric profiles with general features captured by both observing techniques, suggesting these may be real characteristics of the shower and likely not features introduced by observational effects. We point out however that without an in-depth flux computation we are limited in the final conclusions that can be drawn from the activity profiles. For instance, double peaked profiles are more evident in CAMS detected shower, but some of those may be on account of weather.

For the Orionids, both CAMS and SAAMER-OS capture double peaked profiles remarkably similar. These profiles could be caused by nodal dispersion of meteoroids but the mechanism driving the scattering of meteoroids remains unclear. These profiles may suggest a mass-independent mechanism affecting the meteoroid stream. One possible explanation can be due to meteoroids trapped in the 1:6 mean motion resonance with Jupiter (Sato and Watanabe, 2007; Sekhar and Asher, 2014).

For half of the showers in Table 2, the profiles for optically detected showers tend to lag a few degrees in λ_0 behind those observed with radar. In particular, our analysis of the STA, shows that the peak day of optical and radar-based observations are 8° apart. This might signal a potential limitation in our analysis in a region with close nearby showers. This could be particularly relevant for the STA with more than 10 components identified in video observations (Jenniskens et al., 2016b). It is likely that the $xi-$ Arietids (XAR), at α_g ¼ 39:1°, δ_g ¼ 10:5°, $\lambda_g - \lambda_0$ ¼ 194:6°, β_g ¼ −4:6° and v_g ¼ 28:5 km s^{-1} was identified at λ_0 ¼ 205° by the wavelet analysis.

Figs. 20 and 21 illustrate the chain of radiants from the linking methodology for the η-Aquariids and the Orionids with CAMS (red dots) and SAAMER-OS (orange). We plot CAMS detected meteors color-coded by radiant density and plot the excursion of wavelet radiants on top. The wavelet-based linked procedure highlights the evolution of the ETA towards the north advancing along a feature reminiscent of the Orionid tail. The linking procedure captures radiants along the Orionid tail well on CAMS whereas radar radiants are strictly limited to the core of the shower.

5. Conclusions

We have presented the first wavelet transform-based analysis applied to meteor showers detected with the CAMS survey and used the existing SAAMER-OS meteor catalog to compare twenty showers as seen by both surveys. Using 5:7×10^6 radar meteoroid orbits and 471,582 optical meteor detections, we were able to characterize twenty showers following the same analysis methodology.

We developed a deceleration correction for SAAMER-OS detected meteors based on the existing correction from CMOR and reduced the average difference in shower speeds between radar surveys to 0.4 km s^{-1}.

On average, shower positions from the SAAMER-OS and CAMS surveys are 1° apart and 66% have speeds within 1.1 km s^{-1}. Meteor shower reach their peak activity within 1° (median) and 77% of them within 2° apart.

We do see some significant differences in the distribution of dust of small (SAAMER-OS) and large (CAMS) sizes that could signify size-dependent meteoroid stream dynamics. Roughly 50% of showers display seemingly mirrored activity profiles with time while video observed showers tend to lag behind the occurrence of peak activity as detected by SAAMER-OS. The SDA, SZC, and NZC are good examples of the differences in peak activity. All showers with short perihelion distance, where Earth intersects the streams far from perihelion at high mean anomaly. On the other hand, such difference in peak activity is not observed for the ARI. That may be because the Marsden sungrazers have a node passing very close to Earth's.

Features observed in the activity profile of the ARI, CAP, ETA, SDA and ORI are captured by both radar and optical techniques and they might be real features of these meteoroid streams. We emphasize however that a flux computation is required to properly characterize shower profiles and features.

The video-derived radiant dispersion is consistently lower than in radar observations with wavelet probe sizes a factor of 2 smaller on average. The wavelet-based derived radar dispersion has a lower limit of 2.4° and thus it may not be sufficiently low to measure true radiant dispersions.

Most orbital elements from both surveys are similar and consistent with the shower radiant and speeds derived from the wavelet transform analysis and agree with those found in the literature.

CRediT authorship contribution statement

Juan Sebastián Bruzzone: Methodology, Software, Formal analysis, Writing - original draft, Visualization, Conceptualization, Supervision. Diego Janches: Funding acquisition, Resources, Conceptualization, Data curation, Writing - review & editing, Supervision. Peter Jenniskens: Data curation, Resources, Writing - review & editing. Robert Weryk: Software, Writing - review & editing, Data curation. Jose Luis Hormaechea: Data curation.

Acknowledgements

We thank the referees for the insightful comments and suggestions. JSB and D.J.'s work is supported by the NASA SSO and ISFM Programs

and the NASA NESC. SAAMER's operation is supported by NASA SSO, NESC assessment TI-17-01204, and NSF grant AGS-1647354. The authors appreciate the invaluable support of Carlos Ferrer, Gerardo Connon, and Luis Barbero with the operation of SAAMER. PJ acknowledges support from NASA grant 80SSC19K0563 and support from the NASA Goddard Space Flight Center.

Appendix A. Supplementary data

Supplementary data to this article can be found online at https://doi.org/10.1016/j.pss.2020.104936.

References

Baggaley, W.J., Bennett, R.G.T., Steel, D.I., Taylor, A.D., 1994. The advanced meteor orbit radar facility - AMOR. qjras 35, 293.

Brown, P., Jones, J., Weryk, R.J., Campbell-Brown, M.D., 2004. The velocity distribution of meteoroids at the Earth as measured by the Canadian meteor orbit radar (CMOR). Earth Moon Planets 95, 617–626. https://doi.org/10.1007/s11038-005-5041-1.

Brown, P., Weryk, R.J., Wong, D.K., Jones, J., 2008. A meteoroid stream survey using the Canadian Meteor Orbit Radar. I. Methodology and radiant catalogue. Icarus 195, 317–339. https://doi.org/10.1016/j.icarus.2007.12.002.

Brown, P., Wong, D.K., Weryk, R.J., Wiegert, P., 2010. A meteoroid stream survey using the Canadian Meteor Orbit Radar. II: identification of minor showers using a 3D wavelet transform. Icarus 207, 66–81. https://doi.org/10.1016/j.icarus.2009.11.015.

Bruzzone, J.S., Brown, P., Weryk, R.J., Campbell-Brown, M.D., 2015. A decadal survey of the Daytime Arietid meteor shower using the Canadian Meteor Orbit Radar. mnras 446, 1625–1640. https://doi.org/10.1093/mnras/stu2200.

Fritts, D.C., Janches, D., Iimura, H., Hocking, W.K., Mitchell, N.J., Stockwell, R.G., Fuller, B., Vand epeer, B., Hormaechea, J., Brunini, C., Levato, H., 2010. Southern Argentina Agile Meteor Radar: system design and initial measurements of large-scale winds and tides. J. Geophys. Res. C Oceans Atmos. 115, D18112. https://doi.org/10.1029/2010JD013850.

Galligan, D.P., Baggaley, W.J., 2002. Wavelet enhancement for detecting shower structure in radar meteoroid data I. methodology. In: Green, S.F., Williams, I.P., McDonnell, J.A.M., McBride, N. (Eds.), IAU Colloq. 181: Dust in the Solar System and Other Planetary Systems, ume 15, 42.

Galligan, D.P., Baggaley, W.J., 2004. The orbital distribution of radar-detected meteoroids of the Solar system dust cloud. mnras 353, 422–446. https://doi.org/10.1111/j.1365-2966.2004.08078.x.

Galligan, D.P., Baggaley, W.J., 2005. The radiant distribution of AMOR radar meteors. mnras 359, 551–560. https://doi.org/10.1111/j.1365-2966.2005.08918.x.

Gural, P.S., 1995. Applying state-of-the-art video and computer technology to meteor astronomy. WGN, Journal of the International Meteor Organization 23, 228–235.

Gural, P.S., 1997. An operational autonomous meteor detector: development issues and early results. *WGN*. Journal of the International Meteor Organization 25, 136–140.

Gural, P.S., 2012. A new method of meteor trajectory determination applied to multiple unsynchronized video cameras. Meteoritics Planet Sci. 47, 1405–1418. https://doi.org/10.1111/j.1945-5100.2012.01402.x.

Hawkins, G.S., 1963. The Harvard radio meteor project. Smithsonian Contrib. Astrophys. 7, 53.

Hocking, W.K., Fuller, B., Vandepeer, B., 2001. Real-time determination of meteor-related parameters utilizing modern digital technology. J. Atmos. Sol. Terr. Phys. 63, 155–169. https://doi.org/10.1016/S1364-6826(00)00138-3.

Hocking, W.K., Thayaparan, T., Jones, J., 1997. Meteor decay times and their use in determining a diagnostic mesospheric Temperature-pressure parameter: methodology and one year of data. grl 24, 2977–2980. https://doi.org/10.1029/97GL03048.

Jacchia, L.G., Whipple, F.L., 1961. Precision orbits of 413 photographic meteors. Smithsonian Contrib. Astrophys. 4, 97–129.

Janches, D., Close, S., Hormaechea, J.L., Swarnalingam, N., Murphy, A., O'Connor, D., Vand epeer, B., Fuller, B., Fritts, D.C., Brunini, C., 2015. The southern Argentina agile MEteor radar orbital system (SAAMER-OS): an initial sporadic meteoroid orbital survey in the southern sky. APJ (Acta Pathol. Jpn.) 809, 36. https://doi.org/10.1088/0004-637X/809/1/36.

Janches, D., Hocking, W., Pifko, S., Hormaechea, J.L., Fritts, D.C., Brunini, C., Michell, R., Samara, M., 2014. Interferometric meteor head echo observations using the Southern Argentina Agile Meteor Radar. J. Geophys. Res. C Oceans Atmos. 119, 2269–2287. https://doi.org/10.1002/2013JA019241.

Jenniskens, P., 1994. Meteor stream activity I. The annual streams. aap 287, 990–1013.

Jenniskens, P., 2006. Meteor Showers and Their Parent Comets. Cambridge University Press. https://doi.org/10.1017/CBO9781316257104.

Jenniskens, P., 2008. Meteoroid streams that trace to candidate dormant comets. Icarus 194, 13–22.

Jenniskens, P., Baggaley, J., Crumpton, I., Aldous, P., Gural, P.S., Samuels, D., Albers, J., Soja, R., 2016a. A surprise southern hemisphere meteor shower on New-Year's Eve 2015: the Volantids (IAU#758, VOL). *WGN*. Journal of the International Meteor Organization 44, 35–41.

Jenniskens, P., Baggaley, J., Crumpton, I., Aldous, P., Pokorny, P., Janches, D., Gural, P.S., Samuels, D., Albers, J., Howell, A., Johannink, C., Breukers, M., Odeh, M., Moskovitz, N., Collison, J., Ganju, S., 2018. A survey of southern hemisphere meteor showers. planss 154, 21–29. https://doi.org/10.1016/j.pss.2018.02.013.

Jenniskens, P., Duckworth, H., Grigsby, B., 2012. Daytime Arietids and marsden sunskirters (ARI, IAU #171). *WGN*. Journal of the International Meteor Organization 40, 98–100.

Jenniskens, P., Gural, P.S., Dynneson, L., Grigsby, B.J., Newman, K.E., Borden, M., Koop, M., Holman, D., 2011. CAMS: cameras for Allsky Meteor Surveillance to establish minor meteor showers. Icarus 216, 40–61. https://doi.org/10.1016/j.icarus.2011.08.012.

Jenniskens, P., Nénon, Q., Albers, J., Gural, P.S., Haberman, B., Holman, D., Morales, R., Grigsby, B.J., Samuels, D., Johannink, C., 2016b. The established meteor showers as observed by CAMS. Icarus 266, 331–354. https://doi.org/10.1016/j.icarus.2015.09.013.

Jones, J., Webster, A.R., Hocking, W.K., 1998. An improved interferometer design for use with meteor radars. Radio Sci. 33, 55–65. https://doi.org/10.1029/97RS03050.

Kaiser, T.R., Singer, S.F., 1956. Meteors: proceedings of a symposium on meteor physics. Phys. Today 9, 31. https://doi.org/10.1063/1.3060002.

Nesvorny, D., Jenniskens, P., Levison, H., Bottke, W.F., Vokrouhlicky, D., Gounelle, M., 2010. Cometary origin of the zodiacal cloud and carbonaceous micrometeorites. Implications for hot debris disks. Astrophyscial Journal 713, 816–836.

Pokorný, P., Janches, D., Brown, P.G., Hormaechea, J.L., 2017. An orbital meteoroid stream survey using the Southern Argentina Agile MEteor Radar (SAAMER) based on a wavelet approach. Icarus 290, 162–182. https://doi.org/10.1016/j.icarus.2017.02.025.

Sato, M., Watanabe, J.-I., 2007. Origin of the 2006 Orionid Outburst 59, L21. https://doi.org/10.1093/pasj/59.4.L21.

Schult, C., Brown, P., Pokorný, P., Stober, G., Chau, J.L., 2018. A meteoroid stream survey using meteor head echo observations from the Middle Atmosphere ALOMAR Radar System (MAARSY). Icarus 309, 177–186. https://doi.org/10.1016/j.icarus.2018.02.032.

Sekanina, Z., Chodas, P.W., 2005. Origin of the marsden and kracht groups of sunskirting comets. I. Association with comet 96P/Machholz and its interplanetary complex. apjs 161, 551–586. https://doi.org/10.1086/497374.

Sekhar, A., Asher, D.J., 2014. Resonant behavior of comet Halley and the Orionid stream. Meteoritics Planet Sci. 49, 52–62. https://doi.org/10.1111/maps.12117/Xiv:1303.2928.

Verniani, F., 1973. An analysis of the physical parameters of 5759 faint radio meteors. jgr 78, 8429–8462. https://doi.org/10.1029/JB078i035p08429.

Vondrak, T., Plane, J.M.C., Broadley, S., Janches, D., 2008. A chemical model of meteoric ablation. Atmos. Chem. Phys. 8, 7015–7031.

Weryk, R.J., Brown, P.G., 2012. Simultaneous radar and video meteors—I: metric comparisons. planss 62, 132–152. https://doi.org/10.1016/j.pss.2011.12.023.

Whipple, F.L., Jacchia, L.G., 1957. Reduction methods for photographic meteor trails. Smithsonian Contrib. Astrophys. 1, 183–206.